

EARLY ONLINE RELEASE

This is a PDF of a manuscript that has been peer-reviewed and accepted for publication. As the article has not yet been formatted, copy edited or proofread, the final published version may be different from the early online release.

This pre-publication manuscript may be downloaded, distributed and used under the provisions of the Creative Commons Attribution 4.0 International (CC BY 4.0) license. It may be cited using the DOI below.

The DOI for this manuscript is

DOI:10.2151/jmsj.2023-020

J-STAGE Advance published date: May 16th, 2023

The final manuscript after publication will replace the preliminary version at the above DOI once it is available.

1
2
3
4
5
6
7
8
9
10
11
12
13
14
15
16
17
18
19
20
21
22
23
24
25
26

**A Study on Analysis Setting Optimization of Ship-Based
GNSS Measurements for Maritime Precipitable Water
Vapor Monitoring**

Yoshinori SHOJI¹

Meteorological Research Institute, Tsukuba, Japan

Jinya MIURA

Japan Meteorological Agency, Tokyo, Japan

Shuji TSUBAKI

Japan Meteorological Agency, Tokyo, Japan

Yoshikazu HIGASHI

Japan Meteorological Agency, Tokyo, Japan

Sho HIBINO

Japan Meteorological Agency, Tokyo, Japan

Atsushi KOJIMA

Japan Meteorological Agency, Tokyo, Japan

Tetsuya NAKAMURA

27
28
29
30
31
32
33
34
35
36
37
38
39
40
41
42
43
44
45
46
47
48
49
50
51
52
53
54
55
56
57
58
59
60
61

Japan Meteorological Agency, Tokyo, Japan

Keizo SHUTTA

Japan Meteorological Agency, Tokyo, Japan

- Ver. 1, September 09, 2021
- Ver. 2, January 10, 2022
- Ver. 3, March 31, 2022
- Ver. 4, October 24, 2022
- Ver. 5, February 12, 2023
- Ver. 6, April 06, 2023
- Ver. 7, April 21, 2023

1) Corresponding author: Yoshinori Shoji, Meteorological Research Institute, 1-1,
Nagamine, Tsukuba, Ibaraki 305-0052 JAPAN
Email: yshoji@mri-jma.go.jp
Tel: +81-29-853-8552

62

63

Abstract

64

65 We performed kinematic precise point positioning (PPP) to determine the optimum
66 analysis settings for precipitable water vapor (PWV) retrieval at sea using a ship-based
67 Global Navigation Satellite System (GNSS). Three analysis parameters were varied: the
68 standard deviation of random walk process noise (RWPN) of Zenith Total Delay (ZTD)
69 time variation, the analysis time width, and the time interval of update of the Kalman filter
70 state vector. A comparison with the Meso-scale Analysis (MA) of the Japan Meteorological
71 Agency revealed that, depending on the update interval and the time width, a
72 strengthened RWPN constraint suppresses the unnatural time variation of GNSS-derived
73 PWV, reduces negative bias against MA, but decreases the regression coefficient.

74 On the basis of the results of comparison of GNSS-derived PWV with MA, a setting
75 combination of $3 \times 10^{-5} \text{ m s}^{-1/2}$, 1.5 h, and 2 s for the RWPN, the time width, and the
76 update interval, respectively, was selected to compare with other observations. Biases
77 and root-mean-square differences between the ship-based GNSS-derived PWV and
78 radiosonde observation, a nearby ground-fixed GNSS station, and a satellite-borne
79 microwave radiometer were -0.48 and 1.75 , 0.08 – 0.25 and 1.49 – 1.63 , and 1.04 – 1.18
80 and 2.17 – 2.43 mm, respectively.

81 The factors yielding the differences in the GNSS-derived PWV bias were discussed,
82 especially the errors in the estimated GNSS antenna altitude. The error in the vertical
83 coordinate in GNSS positioning was confirmed as negatively correlated with the error in
84 the GNSS-derived PWV. We found that the kinematic PPP is more likely to overestimate
85 the altitude with shorter update intervals and wider time widths. When the RWPN and the
86 update interval were set to $3 \times 10^{-5} \text{ m s}^{-1/2}$ and 2 s, respectively, the bias of the analyzed
87 altitudes by the kinematic PPP changed from negative to positive at approximately 1 h
88 width. The results suggest that precise GNSS positioning is necessary for accurate
89 GNSS-derived PWV analysis.

90

91 **Keywords** GNSS; water vapor; maritime observation; kinematic positioning

92

93 **1. Introduction**

94 Water vapor monitoring over the ocean has become an important issue in Japan, an
95 archipelago located east of East Asia, following the increased frequency of extreme
96 precipitation events. Japan is influenced by the East Asian monsoon, characterized by moist
97 air inflow from the ocean that often causes heavy rainfall (Kato 2006, Tsuguti and Kato 2014,
98 Kato 2018). Imada et al. (2020) applied large-ensemble simulations of the general circulation
99 model and downscaled high-resolution products with a 20 km non-hydrostatic regional
100 climate model to show that anthropogenic warming increased the risk of two record-breaking
101 regional heavy rainfall events in 2017 and 2018 over western Japan. Their findings showed
102 that both episodes were induced by an abnormal moisture inflow toward a stationary
103 rainband in the coastal regions of Japan's Inland Sea and the west side of the mountain
104 range on the main island of Kyushu, respectively. Furthermore, Shoji et al. (2009) exhibited
105 an improvement in heavy rainfall prediction by assimilating precipitable water vapor (PWV)
106 which has been estimated via the Global Positioning System (GPS) observation network in
107 East Asia and Japan's nationwide dense GPS network, indicating the importance of
108 upstream water vapor monitoring.

109 Major maritime water vapor observation tools include the satellite-borne microwave
110 radiometer (MWR) and the atmospheric infrared sounder. They are both affected by
111 raindrops and the Earth's surface (Zhou et al. 2016) and are influenced by cloud coverage,

112 especially in the lower troposphere. Advanced geostationary meteorological satellites
113 (Meteosat, Himawari, and GOES) are equipped with water vapor channels to observe water
114 vapor distribution in the middle and upper troposphere (Bessho et al. 2016). However, water
115 vapor distribution in the lower troposphere was hardly observed. No observational system
116 can continuously monitor maritime water vapor under all weather conditions.

117 Since the start of GPS use in 1993, it has become a fundamental infrastructure in our daily
118 lives. Currently, the European Union and several countries have satellite positioning and
119 navigation systems, more commonly referred to as the Global Navigation Satellite System
120 (GNSS).

121 The basic concept of GNSS positioning is range measurement between satellites and
122 receivers, using time of GNSS signals to reach the receivers. The GNSS signals are delayed
123 and signal propagation paths are bent due to changes in air density. In precise GNSS
124 positioning, tropospheric delay, which is the integrated refractivity along the signal path, is
125 estimated as one of the unknown parameters. Refractivity is a function of temperature,
126 pressure, and vapor pressure. In the late 1980s, a new research field called GPS
127 meteorology was introduced, which utilizes estimated tropospheric delays for atmospheric
128 remote sensing (Davis et al. 1985, Askne and Nordius 1987).

129 The GNSS atmospheric sensing methods can roughly be classified into two types; the first
130 utilizes data by ground-based GNSS receivers to retrieve the PWV above each receiver,

131 while the second, the GNSS radio occultation (RO), monitors the vertical profile of
132 atmospheric refractivity by applying ray bending originated when the radio path between a
133 GNSS satellite and receiver installed in a low Earth orbit (LEO) traverses the Earth's
134 atmosphere. The recent FORMOSAT-7/COSMIC-2 (F7/C2) mission launched six LEO
135 satellites in June 2019 and achieved full operational capability on October 12, 2021. Its
136 mission is to provide more than 5000 neutral atmosphere RO profiles daily (Weiss et al.
137 2022). As of October 2022, in addition to F7/C2, several public institutions and private
138 sectors are conducting GNSS RO observations.

139 Shoji (2009) developed a near real-time ground-based GPS data analysis procedure in
140 Japan. The comparison with radiosonde observations (RAOB) launched at nearby GPS
141 stations revealed that the retrieved GPS PWV in near real-time agrees with RAOB, with a
142 bias and root-mean-square (RMS) difference of +0.30 and 1.64 mm, respectively for January
143 2007, and +0.22 and 3.36 mm respectively for July 2007. In October 2009, the Japan
144 Meteorological Agency (JMA) initiated its operational GNSS-derived PWV estimation and its
145 assimilation into the mesoscale objective analysis (MA), with the cooperation of the
146 Geospatial Information Authority of Japan (GSI), which operates the nationwide dense
147 GNSS network, known as GNSS Earth Observation Network (GEONET). Recent hazardous
148 rainfalls have attracted significant attention for water vapor monitoring at sea. Therefore, if
149 PWV is continuously analyzed at sea, it would contribute to heavy rainfall prediction.

150 Research on PWV retrieval using GNSS RO has been conducted (Wick et al. 2008, Huang
151 et al. 2013, Teng et al. 2013, Burgos et al. 2018, Zhang et al. 2018). Burgos et al. (2018)
152 compared PWV retrieved from GNSS RO and ground-based GNSS over ocean-dominated
153 regions, and exhibited a mean difference and an RMS of about 1 and 5 mm, respectively.
154 However, not all GNSS RO-retrieved profiles reach the ground. Consequently, the
155 corresponding uncertainty is inevitable. Furthermore, as Wick et al. (2008) stated, the spatial
156 resolution of each GNSS RO-retrieved PWV is approximately 250 km along the ray path
157 and 1 km across the path.

158 The first challenge in maritime PWV estimation using a floating-platform GPS was reported
159 by Chadwell and Bock (2001). Since then, related studies have been published over several
160 years (Rocken et al. 2005, Fujita et al. 2008, Boniface et al. 2012, Fujita et al. 2020). Kato
161 et al. (2018) mentioned the possibility of utilizing a floating-buoy-mounted GNSS for
162 synthetic geohazard monitoring, such as tsunami and heavy rainfall potential. Several
163 studies discussed the potential of ship-based GNSS-derived PWV to improve numerical
164 weather prediction (NWP). Boniface et al. (2012) concluded that GPS PWV measured
165 aboard ships for data assimilation (DA) applications should bring constraints in NWP
166 analyses, considering the results of a four-month shipborne GPS observation campaign
167 conducted in the Mediterranean Sea in the autumn of 2008. Ikuta et al. (2021) assimilated
168 PWVs observed by GNSS onboard ships to show their impact on a heavy rainfall event in

169 July 2020 and successfully improved rainfall prediction accuracy.

170 Inspired by the increasing number of GNSS satellites and the advancement of real-time
171 kinematic positioning technology, operational PWV estimation using a floating-platform
172 GNSS has become increasingly common. Shoji et al. (2016) and Shoji et al. (2017) used
173 real-time GNSS satellite ephemerides named Multi-GNSS Advanced Demonstration tool for
174 Orbit and Clock Analysis (MADOCA; Kogure et al. 2016) in their postprocessing PWV
175 retrieval experiments using ship-based GNSS measurements. Shoji et al. (2017) compared
176 the vessel-borne GNSS-derived PWV and RAOB and found that both agreed very well, with
177 1.7 mm RMS differences and a -0.7 mm mean deviation. However, GNSS-derived PWV
178 showed unnatural time fluctuations with a cycle of several hours in their analyses.
179 Consequently, quality control was performed to reject cases where the time change of Zenith
180 Total Delay (ZTD) time change was larger than 0.1 mm/s. Through the quality control
181 procedure, 3.6% of the retrieved PWVs were rejected before the comparison with RAOBs.
182 The authors also found a growing negative bias of GNSS-derived PWV under high PWV
183 circumstances. They speculated that this might be due to the growing difficulty in separating
184 the signal delay and vertical coordinate under high-humidity conditions. Dee (2005) noted
185 that the DA theory is primarily concerned with optimally combining model predictions with
186 observations in the presence of random, zero-mean errors. The presence of biases means
187 the available data was not used optimally.

188 This research attempts to modify some analysis options to discover a way to reduce
189 unnatural fluctuations and negative bias of ship-based GNSS-derived PWVs that increase
190 under high PWV circumstances observed by Shoji et al. (2017). Section 2 describes the
191 experiment for determining the optimum analysis settings for the ship-based GNSS analysis.
192 Section 3 compares the ship-based GNSS-derived PWV by the new settings with other
193 observational data and the PWV by the settings of Shoji et al. (2017). Section 4 discusses
194 the factors leading to the differences in the results described in Sections 2 and 3, especially
195 regarding errors in the estimated GNSS antenna altitude. The paper closes with a summary
196 and conclusions in Section 5. The Appendix outlines our ship-based real-time GNSS
197 observation and analysis system of maritime PWV.

198

199 **2. Determination of the Optimal Analysis Procedure**

200

201 The GNSS analysis procedure adopted in this study is in line with the study by Shoji et
202 al. (2017) (Table 1). Kinematic precise point positioning (PPP) (Zumberge et al. 1997) is
203 executed using a GNSS analysis library named RTKLIB (Takasu 2013) and by applying the
204 MADOCA real-time product. The RTKLIB employs an Extended Kalman Filter (EKF) to
205 estimate unknown parameters, including GNSS antenna coordinates and ZTD, which is
206 modeled as a random walk variable. The following three settings (Table 1) have been

Table 1

207 examined: the standard deviation of Random walk Process Noise (RWPN) of ZTD time
208 variation, time width of the sliding window, and the time interval of update of the EKF state
209 vector, which was determined by the sampling rate (observation recording interval).

210 Zumberge et al. (1997) found that treating ZTD time variation as a stochastic process is
211 effective. The RWPN sigma constrains the degree of ZTD time variation. Optimum time ZTD
212 constraint should be geographically and timely dependent. Several studies modeled ZTD as
213 a random walk process and used their own RWPN settings, ranging from 0.3×10^{-5} - 33.3
214 $\times 10^{-5} \text{ m s}^{-1/2}$ (Table 2). The RTKLIB default RWPN sigma value is $10.0 \times 10^{-5} \text{ m s}^{-1/2}$, which
215 is set as a value that empirically gives the best result of the positioning solution. Vaclavovic
216 et al. (2017) examined the impacts of the RWPN sigma of ZTD on estimated unknown
217 parameters and observed a significant negative correlation between the estimated height
218 and ZTD. They concluded that a careful offline analysis of an optimal RWPN setting for an
219 estimated ZTD should be performed to achieve the best accuracy. Hadas et al. (2017)
220 proposed using NWP models to define optimum RWPN settings.

Table 2

221 There are two options for real-time analysis: true real-time analysis, which continuously
222 updates the forward analysis using information such as satellite orbit and carrier phase
223 obtained in real-time, or rapid update of sliding-window analysis (Foster et al. 2005), which
224 frequently performs batch processing while updating the analysis target time. Figures 1 (a)
225 and (b) illustrate the differences between the two analysis procedures. Figure 1(a) is superior

Fig. 1

226 regarding computer load compared to (b) due to multiple estimation of time-dependent
227 parameters at each epoch in (b). If the positioning accuracy improves or does not change
228 with wider time width, then (a) is the best option. When performing the sliding-window
229 analysis, appropriately determining the width of the sliding-window is necessary. The PPP
230 analysis needs an order of tens of minutes of data to reach a converged solution (Choy et
231 al. 2017). However, the wider the time width, the higher the computational cost. Foster et al.
232 (2005) chose 8-h width to effectively compromise the processing time and solution accuracy.
233 Shoji et al. (2017) adopted a traditional 24-h-batch approach (Fig. 1(c)), but with an extra 3
234 h of data added before each 24-h data file to avoid using unconverged solutions.

235 Several studies suggested a high rate of up to 10 Hz for the GNSS analysis to monitor
236 the dynamic behavior of engineering structures and seismology (Wang et al. 2012, Xu et al.
237 2013). However, Erol et al. (2020) investigated the effect of different sampling interval on
238 the PPP solutions and found that higher sampling rates produced solutions with relatively
239 poor quality in kinematic PPP results. According to them, this could be due to the high
240 temporal correlation between observations with a higher sampling rate caused by multipath
241 and atmospheric errors.

242 The above three parameters may have different effects on GNSS analysis, depending on
243 their combination. However, partly due to the computational load, a statistical inspection of
244 all combinations is difficult. First, we selected the optimal RWPN setting. Second, we

245 examined the combined effects of time width and update interval.

246 In Section 2, we compared the ship-based GNSS-derived PWV with those calculated from
247 Grid Point Value (GPV) of MA. There was no combination of settings with the best
248 agreement on following all three measures: the regression coefficient of the linear regression
249 line, bias, and standard deviation (SD) of the differences. Subsequently, to compare with
250 other observations in Section 3, we selected one set of the RWPN, the time width, and the
251 update interval that resulted in one of the good agreements with MA.

252

253 *2.1 Observation and PWV retrieval*

254

255 Table 3 summarizes vessel sizes, weights, GNSS antennas, and receiver types. It
256 displays the GNSS antenna on each vessel used herein. We conducted ship-based GNSS
257 observations on one research vessel, Ryofu Maru, and two cargo ships, Wakanatsu, and
258 Ryuunan, starting in December 2018. We initially set the evaluation period to about one
259 month around the Japanese rainy season, June 15-July 15, 2020. Unfortunately, we could
260 not conduct high-sampling observations on Ryofu Maru for operational reasons. As an
261 alternative, we executed 10 Hz GNSS observations on Wakanatsu and Ryuunan from
262 October 22 to November 20, 2020.

Table 3

263 To acquire the ZTD time series every 30 min, using RTKLIB, kinematic PPP analyses with

264 the sliding-window method were conducted. To calculate PWV from ZTD, Zenith Hydrostatic
 265 Delay (ZHD) was obtained, following Elgered et al. (1991), as a function of the pressure,
 266 latitude (φ), and altitude (ht) of the GNSS antenna.

$$267 \quad ZHD(P, \varphi, ht) = \frac{2.2779 \cdot P}{1 - 0.00266 \cdot \cos 2\varphi - 0.00028 \cdot ht} \quad (1)$$

268 As a next step, the zenith wet delay (ZWD) is derived by subtracting ZHD from ZTD.

$$269 \quad ZWD = ZTD - ZHD \quad (2)$$

270 Finally, PWV was estimated from ZWD using a conversion coefficient (Π) (Askne and
 271 Nordius 1987).

$$272 \quad PWV = \Pi \cdot ZWD, \quad (3)$$

$$273 \quad \Pi = \frac{10^5}{R_v \left(-k_1 \frac{M_w}{M_d} + k_2 + \frac{k_3}{T_m} \right)}, \quad (4)$$

274 where R_v , M_w , and M_d are gas constant for water vapor, molecular weight of water vapor,
 275 and molecular weight of dry air. k_1 , k_2 , and k_3 are empirical constants for refractivity
 276 formula. T_m indicates the mean temperature of the atmospheric column weighted by the
 277 amount of water vapor defined by Davis et al. (1985).

$$278 \quad T_m = \frac{\int_H^{\infty} \frac{P_v}{T} dz}{\int_H^{\infty} \frac{P_v}{T^2} dz}, \quad (5)$$

279 where H , T , and P_v are GNSS antenna height, temperature, and vapor pressure,
 280 respectively. Bevis et al. (1992) indicated that T_m correlates with surface temperature.

281 This parameter is estimated from the interpolated surface temperature, using a linear
 282 relation between T_m and surface temperature based on one-year statistics of RAOB in

283 Japan.

284 Therefore, to calculate PWV from ZTD obtained in GNSS positioning, P and T value at
285 the GNSS antenna position are required. From Subsection 2.2 to 2.4, MA's GPV
286 interpolated to the GNSS antenna location was used for the P and T values. Section 3
287 used the P and T value observed on each vessel. We compared the PWV calculated
288 using the P and T of MA with those using the observed P and T for one month of April
289 2021. The correlation coefficient of the two sets of PWVs exceeded 0.999, the absolute
290 value of the mean difference was 0.11 mm, and the random difference was 0.2 mm.

291 The PWV of the MA was calculated by vertically integrating specific humidity.

$$292 \quad PWV = \frac{1}{g} \int_{P_s}^{P_t} q dp, \quad (6)$$

293 where q , P , P_t , P_s , and g correspond to specific humidity, pressure, model top pressure,
294 model surface pressure, and gravitational acceleration, respectively.

295

296 *2.2 Examination of RWP setting using Ryofu Maru data*

297

298 To examine the optimal RWP setting, eight GNSS analyses were performed for
299 approximately 1 month (from June 15 to July 15) using 1 Hz-sampled Ryofu Maru data while
300 changing the RWP sigma as 1×10^{-4} , 5×10^{-5} , 3×10^{-5} , and $1 \times 10^{-5} \text{ m s}^{-1/2}$ and the time
301 width of the sliding window as 1.5, and 8.0 h.

302 The RTKLIB default value for RWPN sigma is $1 \times 10^{-4} \text{ m s}^{-1/2}$. The PWV time sequence
303 of Ryofu Maru in Shoji et al. (2017) showed short-term fluctuations, which did not occur for
304 PWV analysis with the static PPP of a nearby ground-based fixed GNSS station. Regarding
305 the suppression of unnatural short-term fluctuations, we examined stronger RWPN
306 constraints, and a detailed evaluation of the influence of the time width is presented in the
307 next section. We compared the results of the two time widths of 1.5 and 8.0 h. The former
308 width was selected because Choy et al. (2017) mentioned that several tens of minutes are
309 needed for PPP to convergence, and the latter was selected on the basis of Foster et al.
310 (2005).

311 Table 4, and the scatter diagrams in Fig. 2 depicts the comparison results of PWVs
312 obtained from the eight experiment analyses against those by MA. To examine the
313 differences in the agreement between cases with high and low PWV, the bias, RMS, and
314 SD were calculated for three bins: (1) all data, (2) PWV <40 mm, and (3) PWV \geq 40 mm. For
315 all data, the RMS difference and SD were smaller in the 1.5 h width, with a combination of
316 the RWPN of $3 \times 10^{-5} \text{ m s}^{-1/2}$. Conversely, the 8.0 h width tended to have larger RMS and
317 SD values. This tendency seems to be stronger in smaller RWPNs. Regardless of the time
318 width of the analysis or the selected RWPN setting, biases were positive for PWV <40 mm
319 and negative for PWV \geq 40 mm. Comparing the RMS of the 1.5 h analysis with that of 8.0 h
320 analysis, both the positive biases for PWV <40 mm and negative biases for PWV \geq 40 mm

Table 4

Fig. 2

321 tend to be closer to zero for the 1.5 h analysis. The selection of smaller RWPN (stronger
322 time constraint) resulted in a larger positive bias for PWV <40mm and smaller negative bias
323 for PWV ≥40 mm. The change in bias caused by using different RWPNs is greater for the
324 8.0 h analysis than for the 1.5 h analysis. As a result, for both 1.5 h and 8.0 h analyses, the
325 selection of smaller RWPN resulted in smaller regression coefficients and larger y-intercepts
326 of linear regression, although it reduced the negative biases of GNSS-derived PWV.
327 Comparing 1.5 and 8.0 h analyses with the same RWPN shows that the former has a larger
328 (closer to 1) regression coefficient and smaller y-intercept than the latter. While increasing
329 the time constraint of the RWPN had a positive effect of reducing the unnatural variability of
330 the analyzed PWV, it also had a negative influence as reducing the regression coefficient
331 and increasing the y-intercept of the linear regression line. Regarding the reduction of RMS
332 in GNSS-derived PWV against MA, we can state that, among these eight experiments, a 1.5
333 h width with an RWPN of $3 \times 10^{-5} \text{ m s}^{-1/2}$ showed the best agreement with MA.

334 The panels in Fig. 3 represent the PWV time series by RAOBs (red dots), expressed in
335 MA (thick gray line) and GNSS-derived PWV (other colored lines). A setting of smaller RWPN
336 increases the suppression of the GNSS-derived PWV time variation, and the tendency is
337 stronger in the results of 8.0 h width than that of 1.5 h width.

Fig. 3

338 Figure 4 shows the differences in the estimated altitude dependent on the time width
339 and the RWPN. The smaller the RWPN, the higher the analyzed altitude, specifically in 8.0

Fig. 4

340 h width analyses. As Vaclavovic et al. (2017) and Shoji et al. (2000) reported, errors in zenith
341 coordinates show a negative correlation with errors in ZTD. Conversely, height
342 overestimation occurs in synchronization with ZTD underestimation. The results shown in
343 Figs. 2–4 indicate that (1) adopting an RWPN smaller than RTKLIB's default value yields
344 smaller RMS and SD of GNSS-derived PWV and (2) a smaller RWPN tends to create
345 positive biases in the zenith coordinate. The biases increase with a wider time width.

346

347 *2.3 Examination of EKF update interval and time width*

348

349 In kinematic PPP with the MADOCA real-time product, 30 to 40 min continuous data are
350 required from the start time for the analysis to converge (Kogure et al. 2016). The sampling
351 interval (time interval of update of EKF state vector) may affect the convergence time and
352 positioning accuracy. Therefore, we experimented with an accuracy comparison using 10
353 Hz observation data while changing the time width and the update interval.

354 From October 22 to November 20, 2020, we conducted a dual-frequency 10 Hz
355 sampling GNSS observations on two cargo ships, Wakanatsu and Ryuunan (Table 2). In the
356 GNSS analysis, the RWPN was fixed at $3 \times 10^{-5} \text{ m s}^{-1/2}$, based on Subsection 2.2.
357 Subsequently, the time width of the sliding window was changed from 0.5 to 8.5 h with a 1
358 h time slot, while the update interval was modified 13 times, from 0.1 to 30 s. Using GNSS-

359 estimated ZTD and the pressure and temperature of MA interpolated at the GNSS antenna
360 position, the GNSS-derived PWV was estimated every 30 min to match the time interval of
361 the MA dataset and subsequently compared with the MA PWV.

362 From the comparison (Fig. 5), we can observe the following characteristics:

Fig. 5

363 (a) The regression coefficient of the linear regression line is the largest when the time
364 width is 1.5 h and the update interval is 20 s. At update intervals exceeding 2 s, the
365 regression coefficient becomes the largest at a time width of 1.5 h, but the regression
366 coefficient becomes smaller as the update interval becomes shorter. The longer the update
367 interval, the greater the regression coefficient change as the time width changes.

368 (b) The y-intercept of the linear regression line also varies with the time width and the
369 update interval. The longer the update interval, the greater the change in the y-intercept with
370 time width. At a time width of 1.5 h, the y-intercept becomes closest to zero (-0.36 mm) at
371 an update interval of 2 seconds and becomes farthest from zero (-0.79 mm) at an update
372 interval of 30 seconds. The longer the update interval, the greater the change in the y-
373 intercept with time width.

374 (c) When the update interval is shorter than 10 s, negative bias increases with
375 decreasing update interval and increasing time width. At a time width of 1.5 h, the negative
376 bias becomes closer to zero than -1 mm when the update interval is between 2 and 15 s
377 and becomes the smallest (-0.89 mm) at an update interval of 4 seconds.

378 (d) SD becomes minimal at a time width of 1.5 h irrespective of the update interval. The
379 longer the update interval, the greater the change in the SD with time width. SD becomes
380 the smallest (1.99 mm) for update intervals of 1 and 2 s.

381 (e) The changes in RMS are similar to those in SD but reflect the influence of bias. The
382 RMS is the smallest (2.19 mm) at an update interval of 4 seconds and the second smallest
383 (2.20 mm) at an update interval of 2 seconds.

384 According to Fig. 5, the optimal time width that will minimize the SD and RMS is 1.5 h.
385 However, determining the optimal update interval is difficult. No setting satisfies both the
386 regression coefficient and y-intercept of the linear regression line. The negative y-intercept
387 values tend to be larger in groups where the regression coefficient is close to 1, so the
388 relative error becomes larger in a smaller PWV environment. Further, the groups that have
389 a regression coefficient close to 1 differ from the groups with smaller bias, smaller SD, and
390 smaller RMS. In this study, we selected an update interval of 2 seconds because with a 2 s
391 update interval, y-intercept and SD values were closest to zero, and RMS was the second
392 closest to zero. With respect to bias, the update interval of 4 seconds is closest to zero. For
393 the 4 s update interval, the regression coefficient was closer to 1 than that for the 2 s update
394 interval, and the RMS was minimal. The choice of update interval may vary between 2 and
395 5 s, depending on which of the five indicators shown in Fig. 5 is considered more important.

396 In summary, we selected the following combination of settings for comparisons with

397 other observations in Section 3: an update interval of 2 seconds, a time width of 1.5 h, and
398 an RWPN sigma of $3 \times 10^{-5} \text{ m s}^{-1/2}$ (red line in Fig. 5).

399

400 **3. Comparison with Other Observation**

401

402 In this section, we present the differences in the results between the method proposed
403 by Shoji et al. (2017) and the combination of settings chosen in Section 2 by comparing
404 PWVs using ship-based GNSS with those using RAOB, a nearby ground-based fixed GNSS,
405 and a satellite-borne microwave radiometer (SMWR).

406 We note that each piece of information has a different spatiotemporal scale when
407 comparing GNSS-derived PWV with other observed or analyzed values. The GNSS-derived
408 PWV can be regarded as an average value in an inverted conical space with a radius of
409 approximately 30 km and the GNSS antenna at its apex. The RAOB data are often used as
410 a reference value for evaluating remote sensing observations. However, it takes
411 approximately 0.5 h to travel through the troposphere. Therefore, compared with RAOB, the
412 GNSS-derived PWVs need to be averaged for approximately 30 min, which may obscure
413 the effect of the unnatural PWV fluctuation mentioned by Shoji et al. (2017). Additionally,
414 after launch, each radiosonde drifts with the wind. The SMWR is a remote sensing
415 instrument for measuring weak microwave emissions from the surface and the atmosphere
416 of the Earth. The SMWR-observed values are considered instantaneous values at the time

417 of observation, and the spatial resolution depends on the observation beam width.

418 When the PWVs of ship-based GNSS are compared with those of RAOB, nearby
419 ground-based fixed GNSS, and SMWR, certain characteristics regarding the ship-based
420 GNSS-derived PWV accuracy are revealed. In the following comparison, we referred to the
421 method of Shoji et al. (2017) as CTL and our method as NEW. To examine the differences
422 in agreement between cases with high and low PWV, bias, RMS, and SD were calculated
423 for three bins: (1) all data, (2) $PWV < 40$ mm, and (3) $PWV \geq 40$ mm.

424

425 *3.1 Comparison with RAOB*

426

427 Figure 6 shows the PWV comparison results from the Ryofu Maru observation in 2019
428 and 2020. A total of 134 RAOBs were compared with the ship-based GNSS-derived PWVs.
429 Following Shoji et al. (2017), GNSS-derived PWVs were time-averaged over 30 min
430 beginning at each radiosonde launch time. Comparing NEW with CTL for all data, RMS and
431 SD decreased by approximately 0.1 mm, although negative bias increased by 0.1 mm. In
432 the bin of $PWV < 40$ mm, the negative bias increased by 0.2 mm, whereas the negative bias
433 decreased by 0.04 mm in the bin of $PWV \geq 40$ mm. As a result, the regression coefficient
434 approached 1, but y-intercept turned negative.

435

436 *3.2 Comparison with a nearby ground-based GNSS station*

Fig. 6

437

438 Between March 22 and 26, 2021, wiring and equipment installation for permanent dual-
439 frequency GNSS observation on two JMA research vessels, Ryofu Maru (call sign JGQH)
440 and Keifu Maru (call sign JPBN), were performed. We started observations on March 26,
441 they are still ongoing as of April 2023. The system overview, data acquisition statistics, and
442 an observation case can be found in the Appendix.

443 The two vessels were anchored side by side at their homeport of Daiba, Tokyo, until
444 they departed on April 7, 2021. From the PWV time sequences from April 1 to 6 (Fig. 7), we
445 confirmed that the PWVs analyzed from both vessels agreed well with those of a nearby
446 ground-based fixed GNSS station (3023) and the MA. The PWVs analyzed from ground-
447 based fixed GNSS observations were assimilated into the MA. With CTL (Fig. 7(b)),
448 fluctuations with a cycle of approximately several hours are conspicuous in the PWV time
449 series of both JGQH and JPBN. The amplitude of the fluctuations often exceeds 5 mm.

Fig. 7

450 For April 1 to July 22, 2021, we compared PWVs of JGQH and JPBN with those of “3023”
451 only when each vessel was within 15 km from “3023.” The results in Fig. 8 indicate that in
452 the comparison of all data, SD and RMS values are closer to zero with the NEW settings.
453 The biases were positive for both JGQH and JPBN. The change in bias of the bin of PWV
454 <40 mm relative to the bin of ≥ 40 mm was -0.64 mm (JPBN) and -0.43 mm (JGQH) for CTL
455 and -0.42 mm (JPBN) and +0.01 mm (JGQH) for NEW. The change in bias dependence on

Fig. 8

456 the PWV is smaller in NEW than in CTL.

457

458 *3.3 Comparison with an SMWR*

459

460 The Global Change Observation Mission (GCOM), a Japan Aerospace Exploration
461 Agency (JAXA) project of long-term observation of environmental changes on Earth,
462 launched its first satellite, GCOM-W1, on May 18, 2012. Advanced Microwave Scanning
463 Radiometer 2 (AMSR2) uses 18.7, 23.8, and 36.5 GHz bands to observe PWV over the
464 ocean for a horizontal resolution of approximately 15 km (Kazumori 2013).

465 We allowed a 5 min difference and a 20 km distance for the matchup, and Fig. 9 shows
466 the comparison results. Concerning GCOM-W1, the GNSS-derived PWV has >1 mm
467 positive biases. Similar to the RAOB and ground-based fixed GNSS comparison, the PWV
468 with NEW results in smaller SD and RMS values than CTL. The change in bias for PWV <40
469 mm and ≥ 40 mm is also -1.90 mm (JPBN) and -1.72 mm (JGQH) for CTL. However, the
470 analysis with NEW showed reduced changes of -1.31 mm (JPBN) and -1.08 mm (JGQH).
471 Similar to the comparison with RAOB and ground-based fixed GNS station, the change in
472 bias dependence on the PWV is smaller in NEW than in CTL.

Fig. 9

473

474 **4. Discussion**

475

476 In Section 3, we found the following:

477 a) The new analysis setting suppresses the unnatural fluctuation of ship-based GNSS-
478 derived PWV observed by Shoji et al. (2017). The comparisons with RAOB, a nearby
479 ground-based fixed GNSS station, and an SMWR show a decrease in RMS and SD except
480 for RAOB with a PWV ≥ 40 mm.

481 b) Bias changes were characterized differently depending on the observations used for
482 comparisons. The negative bias increased by about 0.1 mm in comparison to RAOB, the
483 positive bias increased by 0.01 and 0.16 mm for JPBN and JGQH, respectively, in
484 comparison to a ground-based fixed GNSS station, and the positive bias decreased by 0.13
485 and 0.1 mm in JPBN and JGQH, respectively, in comparison to SMWR. In all of the
486 comparisons, the NEW setting showed smaller bias dependence on the PWV.

487 Herein, we discuss about the bias in GNSS-derived PWV and its relation to the bias in
488 estimated GNSS antenna height.

489 In GNSS positioning, a negative correlation between errors in analyzed heights and
490 those in ZTD exists. Through geometric considerations, Beutler et al. (1987) derived the
491 following relationship between errors in station height and those in ZTD:

$$492 \quad \Delta h = \frac{\Delta ZTD}{\cos(Z_{max})}, \quad (7)$$

493 Where Δh , ΔZTD , and Z_{max} are the error in station height, error in ZTD, and maximum
494 zenith angle (90-elevation angle) of GNSS satellites, respectively. By realistically

495 considering receiver clock errors, Santarre (1991) found that errors in vertical coordinates
496 and ZTD are negatively correlated. Rothacher and Beutler (1998) obtained the same results
497 from independent derivations and analysis of observed data. Shoji et al. (2000) and
498 Vaclavovic et al. (2017) also confirmed the negative correlation between the errors in the
499 station height and ZTD. Here, we discuss the study results regarding the analyzed antenna
500 heights.

501 Figure 10 shows a scatter plot of the analyzed altitude differences (CTL-NEW) and those
502 in PWV for the data plotted in comparison with a nearby ground-based fixed GNSS station
503 “3023” (Fig. 8). The correlation between the altitude and PWV differences was -0.4809 and
504 -0.5072 for JPBN and JGQH, respectively. From the linear regression lines, it was implied
505 that an overestimation in altitude of approximately 10 cm corresponds to an underestimation
506 in PWV of about 1 mm, and vice versa.

Fig. 10

507 Figure 11 shows the difference between the analyzed altitudes by CTL and NEW, using
508 the comparison data of a nearby ground-based fixed GNSS station “3023.” The horizontal
509 axis is the PWV at “3023.” The altitude differences were binned by PWV values at “3023” at
510 20 mm intervals and then averaged at each bin. The numbers at the top of each panel are
511 the average differences in altitude at each bin. Although there is a large variation, an
512 increase in the PWV could elevate the altitudes by CTL more than those by NEW. For JPBN
513 and JGQH, the elevation difference between the bin with a PWV ≥ 40 mm and the bin with a

Fig. 11

514 PWV <20 mm is around 2 cm.

515 Table 5 shows the expected PWV difference by applying the mean height difference
516 between CTL and NEW to the linear regression equations (Fig. 10) for PWV <40 mm and
517 PWV \geq 40 mm, respectively. From Fig. 8, the actual average PWV difference for JPBN was
518 +0.02 mm when PWV <40 mm and -0.20 mm when PWV \geq 40 mm. The expected PWV
519 difference of JPBN (Table 5) (+0.003 mm for PWV <40 mm and -0.235 mm for PWV \geq 40
520 mm) are consistent with the actual values. However, for JGQH, the actual difference is -0.06
521 mm for PWV <40 mm and -0.50 mm for PWV \geq 40 mm, while the expected value is -0.140
522 mm and -0.295 mm respectively. Although there is a common tendency of increasing
523 negative differences with increased PWV, the expected values are not quantitatively
524 consistent with actual PWV differences. Reflected GNSS signal waves in ship-based GNSS
525 observations and changes in phase center due to antenna tilt and rotation may have affected
526 the results. Assessing the effects of these error factors inherent in ship-based GNSS
527 observations is an issue to be addressed in the future.

Table 5

528 To study the relationship between the errors in altitude and PWV, we installed a set of the
529 same type of GNSS antenna and a receiver with that at Keifu Maru in a field at the
530 Meteorological Research Institute (Tsukuba, Ibaraki, Japan) and conducted a 16-day GNSS
531 observation from December 1 to December 16, 2021. We executed both static and kinematic
532 PPP and compared the positioning results. The settings of kinematic PPP were changed as

533 follows: (i) 16 time widths, from 0.5 to 8.5 h, increased by 0.5 h each; (ii) five update intervals,
534 0.1, 1.0, 2.0, 10.0, and 30.0 s; (iii) and two RWPNs, 1×10^{-4} , and $3 \times 10^{-5} \text{ m s}^{-1/2}$. Table 1
535 presents other settings. Additionally, we performed a 16-day static PPP analysis using 24 h
536 batch processing with a precise ephemeris provided by International GNSS Service (IGS).
537 Hereafter we refer the IGS's precise ephemeris as IGF. The update interval was set to 30.0
538 s to match the time interval of clock correction of the IGF, and the RWPN was set in two
539 ways: 1×10^{-4} and $3 \times 10^{-5} \text{ m s}^{-1/2}$.

540 Figure 12 shows the average and SD of the estimated altitudes when the RWPN of Fig. 12
541 kinematic PPP was set to an RTKLIB default value, $1 \times 10^{-4} \text{ m s}^{-1/2}$. The averaged altitude
542 (25396.77 mm) and ± 1 sigma (2.31 mm) altitudes from the static PPP analysis are also
543 shown in the figure. When the time window was 0.5 h, the vertical coordinate average was
544 lower than the average of the static PPP result, and the SD was larger than that of the wider
545 time width. With increasing time width, the vertical coordinate average increases, and the
546 SD reduces. If the update interval is 30 s and the time width is 4 h or above, the average
547 altitude falls within the average altitude ± 1 sigma of the static PPP. For update intervals
548 shorter than 2 s, the analyzed mean altitude tends to increase with a shorter and wider in
549 the update interval and the time width, respectively. The SD of the analyzed altitude shows
550 a smaller change when the time width ≥ 2 h compared to the change when the time width
551 ≤ 1.5 h. Compared to the same time width, the shorter the update interval, the larger the SD.

552 As Erol et al. (2020) noted, a reduced update interval does not necessarily appear to improve
553 the accuracy of the positioning results.

554 Figure 13 is the same as Fig. 12, except that the RWPN is set to $3 \times 10^{-5} \text{ m s}^{-1/2}$. For
555 static PPP with IGF, changing the RWPN to $3 \times 10^{-5} \text{ m s}^{-1/2}$ increased the mean altitude by
556 about 0.5 mm, while the SD of the altitudes was almost the same. However, for update
557 intervals $\leq 2 \text{ s}$, compared to Fig. 12, the analyzed altitude average tended to be higher and
558 SD tended to be smaller for shorter update intervals. For the kinematic PPP with an update
559 interval of 2 seconds (red line), the average altitude with a time width of 1 h is closest to that
560 of the static PPP (thick gray line). The average altitude for the 1.5 h width is 4.8 mm higher
561 than that of the static PPP, and the altitude difference increases to 8.3 mm for the 2.5 h width.
562 The SDs of the altitude were 58.6, 49.8, and 46.3 mm at time widths of 1.0, 1.5, and 2.5 h,
563 respectively.

564 According to Kogure et al. (2016), 30–40 min of continuous data is needed for the
565 kinematic PPP convergence. From Figs. 12(b) and 13(b), for the ship-based GNSS, about
566 2 h of continuous data is required for good convergence. In Fig. 5(c), the SD is minimized
567 for the 1.5 h width. This may be related to two factors: the positive bias in analyzed altitude
568 which increases with time width, and the degree of convergence of the kinematic PPP
569 solution.

570 From Figs 11 and 12, for 1.5 h width, smaller bias can be expected by 10 s update

Fig. 13

571 interval than that of 2 s update interval. It is consistent with the features observed in Fig. 5
572 (c).

573

574 **5. Summary and Conclusions**

575

576 In this research, we investigated the optimal real-time analysis settings for ship-based
577 GNSS-derived PWV using the kinematic PPP function of RTKLIB. The results are
578 summarized as follows:

- 579 1) In kinematic PPP analysis, strengthening the constraint for ZTD time variation by
580 setting the RWPN value up to one-third of the default value of RTKLIB suppresses
581 the unnatural PWV time variation which was observed by Shoji et al. (2017).
582 However, GNSS analysis with a smaller RWPN and longer analysis time resulted in
583 a greater positive bias for PWV <40 mm and greater negative bias for PWV ≥40 mm.
- 584 2) Based on the results obtained by comparison of ship-based GNSS-derived PWV
585 with MA PWV, a combination of an RWPN of $3 \times 10^{-5} \text{ m s}^{-1/2}$, a time width of 1.5 h,
586 and an update interval of 2 seconds were selected to compare with RAOB, nearby
587 ground-based fixed GNSS, and SMWR measurements. Except for the comparison
588 with RAOB when PWV was ≥40 mm, the SD and RMS values were smaller in all
589 three comparisons than those obtained using the method of Shoji et al. (2017). The

590 NEW setting showed a smaller bias dependence on the PWV in all comparisons.
591 Our new analysis setting for ship-based GNSS PWV analysis was shown to reduce
592 the growing negative bias of GNSS PWV under high PWV circumstances which was
593 one of the issues raised by Shoji et al 2017.

594 3) The biases in the GNSS-derived PWV described above were related to the biases
595 in the vertical coordinate solutions using the kinematic PPP analysis. Errors in PWV
596 based on GNSS analysis are negatively correlated with errors in vertical coordinates.
597 In kinematic PPP analysis for a fixed ground-based GNSS station, positive biases
598 occur in the vertical coordinate solution when the time interval of update is <10 s.
599 The biases increase with increasing time width and decreasing RWP. N.
600 Consequently, increased time widths, a strengthened constraint for ZTD time
601 variation, and shorter update intervals may contribute to an increase in the negative
602 bias of PWV.

603 4) For the update interval <10 s, vertical coordinates tend to be underestimated at the
604 initial stage of a kinematic PPP analysis. The analyzed vertical coordinate increases
605 with analysis time and tends to overestimate when the analysis time exceeds
606 approximately 1 h. The SD of the vertical coordinate decreases with analysis time
607 until it reaches approximately 2 h. The time width of 1.5 h was the time when the
608 bias and SD of the vertical coordinate solution were both close to zero.

609 The present study allowed us to improve the method of Shoji et al. (2017) for PWV
610 analysis using ship-based GNSS measurements. We suggest that the improvement in PWV
611 analysis accuracy by ship-based GNSS is closely related to the improvement in vertical
612 positioning accuracy. There is still scope for improvement in the vertical coordinate analysis
613 and atmospheric delay in the kinematic PPP. But we could not find a setting that yields the
614 optimal values for all five measures: regression coefficient, y-intercept, bias, SD, and RMS.
615 We evaluated the results from the analysis with a time width of <9 h, although an increased
616 analysis time width (≥ 24 h) might provide different results. Thus, future research should
617 consider evaluating wider analysis times, including true real-time analysis. The cause of the
618 error and the magnitude of its effect would vary depending on the observation environment,
619 such as multipath, amount of water vapor and inhomogeneity, satellite arrangement, and
620 sea conditions. The optimal PWV analysis setting for ship-based GNSS might differ
621 depending on the above conditions. We think comparing with other observations and with
622 numerical weather models are necessary to find the optimal analysis setting for each
623 observation environment. The present study provides an approach to searching for the
624 optimal setting. The method for the adaptive setting of analysis options according to the
625 observation situations could also be a future research subject.

626

627

628
629
630
631
632
633
634
635
636
637
638
639
640
641
642
643
644
645
646

Acknowledgments

We express our sincere gratitude to two anonymous reviewers and Professor Shunji Kotsuki for their essential comments that enabled us to carefully examine the purpose, procedure, and findings of this study. A part of the RAOB was supported by the Cross-ministerial Strategic Innovation Promotion Program (SIP), “Enhancement of societal resiliency against natural disasters” (Funding agency: Japan Science and Technology Agency), and by JSPS KAKENHI grant 20H02420. The GEONET observation data and IGS precise ephemeris were acquired from the FTP server of the Geospatial Information Authority of Japan (GSI). We would like to thank Japan Fisheries Research and Education Agency, MarusanKaiun Co., Ltd., Ryukyu Kaiun Kaisha, KANIYAKU Co., Ltd. and MKKLINE Co., Ltd. for their cooperation for our ship-based GNSS observations. The authors would like to express their sincere appreciation to those who have made efforts to realize this real-time PWV analysis system over the ocean.

Data Availability Statements

The datasets generated and analyzed in this study are available from the corresponding author upon reasonable request.

647

Appendix:

648 System overview, data acquisition statistics, and observation example for a heavy rain
649 case of our real-time PWV analysis utilizing ship-based GNSS measurements

650

651 1) System overview

652

653 Table A1 summarizes the vessels and equipment used for real-time PWV estimation

TableA1

654 Our real-time positioning analysis at sea was possible since QZSS delivers MADOCA real-
655 time products as one of its positioning signals (L6E). The Global Positioning Augmentation
656 Service Corporation (GPAS) was in charge of producing the MADOCA data delivered by
657 QZSS. We installed Chronosphere-L6 GNSS receivers to receive the QZSS's L6E signal,
658 and decode the MADOCA real-time orbit. The QZSS comprised three satellites in Quasi-
659 zenith Orbits (QZO), and one satellite in Geostationary Orbit (GEO). To lengthen QZSS
660 observation time from Japan, the QZO adopts an asymmetric north-south orbit shaped like
661 a figure "8" centered around 135°E. Three QZO satellites can be observed every 8 h with
662 an elevation angle of 70° or more in the Tokyo metropolitan area. However, as of August
663 2021, MADOCA on the L6E signal is transmitted from one GEO (QZS-3) and two out of
664 three QZOs (QZS-2 and QZS-4), while the first QZO (QZS-1) did not transmit the L6E signal.
665 Therefore, depending on the time of the day, receiving L6E becomes difficult because the

666 elevation angle of all QZSSs (except QZS-1) will be below. The missing rate of the L6E
667 signal increases as the receiver moves away from Japan in a direction other than the south.

668 The PC analysis collects the MADOCA real-time orbit and the career phase from GPS,
669 GLONASS, and QZSS satellites. Following the results described in Section 2, it performs
670 kinematic PPP analysis every 10 min. The RWP, the width of the sliding-window, and the
671 update interval were set as $3 \times 10^{-5} \text{ m s}^{-1/2}$, 1.5 h, and 2 s, respectively. The GNSS analysis
672 was completed within 2 min from the start of each analysis.

673 Both vessels were equipped with JMA-certified meteorological sensors. Using GNSS-
674 estimated ZTD and the observed temperature and atmospheric pressure on board, PWV
675 can be estimated every 10 min with a latency of approximately 2 min.

676

677 2) *Data acquisition statistics*

678

679 Immediately after the system installation, minor corrections were required, such as
680 setting the PC to always operate and acquiring meteorological observation data through the
681 inboard data network. After making those corrections, the GNSS real-time analysis became
682 stable by March 31. Since then, continuous analysis has been carried out regardless of
683 whether vessels were moored or sailing.

684 From July 23 to August 5, a total of 19 d of unscheduled outage and accuracy

685 degradation of MADOCA occurred: According to the GPAS announcement, the cause was
686 a problem in collecting global ground GNSS observation network data, used to analyze
687 GNSS satellite orbits and clocks. In this study, we set the validation period for 113 d from
688 April 1 to July 22.

689 Table A2 summarizes the number and rate of successful PWV analyses and those of
690 missing cases. For Ryofu Maru (JGQH), the most common cause of PWV analysis failure
691 was an unexpected 20 h sleep of PC analysis, followed by the failure to acquire the L6E
692 signal. For Keifu Maru (JPBN), there were many L6E reception failures, which were ~2.5%;
693 there were also 17 cases caused by the unexpected outage of the MADOCA real-time orbit.

TableA2

694 Figure A1 illustrates the retrieved PWV distribution along the trajectories of the two
695 vessels, and the locations where MADOCA acquisition failed. Compared to JGQH, JPBN
696 sailed further north and east of Japan. For both ships, MADOCA acquisition often failed
697 when the ships sailed in these directions. Figure A2 shows that, in JPBN, MADOCA
698 acquisition often fails around 12:00-15:00 UTC. This coincides with when the elevation
699 angles of the two L6E transmitting QZSs (SV02 and SV04) are below 40°. The fact that the
700 L6E signal is not transmitted from the first quasi-zenith satellite (SV01) leads to missing data
701 in a specific time zone, especially for JPBN. The successor to SV01, launched on October
702 26, 2021, is designed to transmit the L6E signal. The number of missing data has been
703 reducing since the operation start of the successor satellite on March 24, 2022.

Fig. A1

Fig. A2

704

705 3) *Heavy rain case between July 9 and July 10, 2021*

706

707 Between July 9 and July 10, there was heavy rain in southern Kyushu. At the Satsuma
708 Kashiwabarū weather station in Kagoshima prefecture in southern Kyushu, 24 h
709 precipitation of 473 mm was recorded until 12:40 (local time, UTC +9 h) on July 10, and
710 heavy rain emergency warnings were issued to Kagoshima, Miyazaki, and Kumamoto
711 prefectures. The JPBN conducted RAOBs at 6 h intervals for 7 d, from July 5 to July 12,
712 including the day with heavy rain. The PWV time sequence shown in Fig. A3 shows a rapid Fig. A3
713 increase in PWV after 18:00 UTC on July 7 and a rapid decrease in the first half of July 10.
714 Fig. A3 also shows the short time variation in PWV, such as a 10 mm decrease followed by
715 an increase of ~5 mm in 6 h from 18:00 UTC on July 9, for which the 6 h interval observation
716 could not be captured. The panels in Fig. A4 show the 20 h time sequence, from 11:00 July Fig. A4
717 9 to 07:00 July 10, 2021, of GNSS-derived PWV and surface meteorological data. The
718 GNSS-derived PWV decreased by 10 mm or more in approximately 2 h from 21:00 to 23:00
719 on the ninth day. When GNSS-derived PWV began to decrease, sharp decreases in
720 temperature and mixing ratio, intensifying precipitation, and a large change in wind direction
721 and speed were observed.

722 Figure A5 shows distributions of 1 h precipitation and PWV at 02:00 (local time, UTC +9 Fig. A5

723 h) on July 10. Heavy rains exceeding 50 mm/h in the southern part of Kyushu were analyzed.
724 Heavy rain areas were channeled to the sea in the west-southwest direction. In GCOM-W1,
725 a region with a PWV of more than 60 mm was detected along the heavy rain area. The JPBN
726 is located near the western end of the heavy rainfall area.

727 These results indicate the potential of the ship-based GNSS measurements to observe
728 PWV at sea with high temporal resolution regardless of rain and to predict heavy rainfall.

729

References

- 730
731
- 732 Askne, J. and H. Nordius, 1987: Estimation of tropospheric delay of microwaves from
733 surface weather data, *Radio Science*, **22**, 379-386.
- 734 Bar-Sever Y. E., P. M. Kroger, J. A. Borjesson, 1998: Estimating horizontal gradients of
735 tropospheric path delay with a single GPS receiver, *J. Geophys. Res.*, **103**, 5019-5035.
- 736 Bessho, K., K. Date, M. Hayashi, A. Ikeda, T. Imai, H. Inoue, Y. Kumagai, T. Miyakawa, H.
737 Murata, T. Ohno, A. Okuyama, R. Oyama, Y. Sasaki, Y. Shimozu, K. Shimoji, Y. Sumida,
738 M. Suzuki, H. Taniguchi, H. Tsuchiyama, D. Uesawa, H. Yokota, R. Yoshida, 2016: An
739 Introduction to Himawari-8/9— Japan's New-Generation Geostationary Meteorological
740 Satellites, *J. Meteor. Soc. Japan*, **94**, 151-183.
- 741 Beutler, G., I. Bauersima, W. Gurtner, M. Rothacher, T. Schildknecht, and A. Geiger, 1988:
742 Atmospheric refraction and other important biases in GPS carrier phase observation,
743 *Atmospheric Effects on Geodetic Measurements, Monograph*, **12**, 15–43, School of
744 Surveying, Univ. of New South Wales, Kensington, Australia.
- 745 Bevis, M., S. Businger T. A. Herring, C. Rocken, R. A. Anthes, R. H. Ware, 1992: GPS
746 meteorology: remote sensing of atmospheric water vapor using the global positioning
747 system, *J. Geophys. Res.*, **97**, 15787–15801.
- 748 Boehm, J., B. Werl, H. Schuh, 2006: Troposphere mapping functions for GPS and very
749 long baseline interferometry from European Centre for Medium-Range Weather

750 Forecasts operational analysis data. *J. Geophys. Res.*, **111**: B02406.

751 Boniface, K., C. Champollion, J. Chery, V. Ducrocq, C. Rocken, E. Doerfinger, P. Collard,
752 2012: Potential of shipborne GPS atmospheric delay data for prediction of
753 Mediterranean intense weather events. *Atmos. Sci. Lett.*, **13(4)**, 250–256.

754 Burgos F. Y., P. Alexander, A. de la Torre, R. Hierro, P. LLamedo, and A. Calori, 2018:
755 Comparison between GNSS ground-based and GPS radio occultation precipitable water
756 observations over ocean-dominated regions, *Atmos. Res.*, **209**, 115-122.

757 Chadwell, C. D., Y. Bock, 2001: Direct estimation of absolute precipitable water in oceanic
758 regions by GPS tracking of a coastal buoy, *Geophys. Res. Lett.*, **28**, 3701–3704.

759 Choy, S., S. Bisnath, and C. Rizos. 2017: Uncovering Common Misconceptions in GNSS
760 Precise Point Positioning and Its Future Prospect, *GPS Solutions*, **21**, 13–22,
761 doi:10.1007/s10291-016-0545-x.

762 Davis, J. L., T. A. Herring, I. I. Shapiro, A. E. E. Rodgers, and G. Elgered, 1985: Geodesy
763 by radio interferometry: Effects of atmospheric modeling errors on estimates of baseline
764 length. *Radio Sci.*, **20**, 1593–1607.

765 Dee, D. P., 2005: Bias and data assimilation, 2005: *Quart. J. Roy. Meteor. Soc.*, 131, 3323-
766 3343, DOI: 10.1256/qj.05.137

767 Elgered, G., J.L. Davis, T. A. Herring, I. I. Shapiro, 1991: Geodesy by radio interferometry:
768 Water vapor radiometry for estimation of the wet delay, *J. Geophys. Res.*, **96**, 6541-
769 6555.

770 Erol, S., R. M. Alkan, İ. M. Ozulu, V. İlçi, 2020: Impact of different sampling rates on
771 precise point positioning performance using online processing service, *Geo-spatial*
772 *Information Science*, DOI: 10.1080/10095020.2020.1842811

773 Foster J., M. Bevis, S. Businger, 2005: GPS Meteorology: Sliding-Window Analysis, *J.*
774 *Atmos. Oceanic Technol.*, **22**, 687-695.

775 Fujita, M., T. Fukuda, I. Ueki, Q. Moteki, T. Ushiyama, and K. Yoneyama, 2020:
776 Experimental Observations of Precipitable Water Vapor over the Open Ocean Collected
777 by Autonomous Surface Vehicles for Real-Time Monitoring Applications, *SOLA*, **16A**, 19-
778 24, doi:10.2151/sola.16A-004.

779 Fujita, M., F. Kimura, K. Yoneyama, M. Yoshizaki, 2008: Verification of precipitable water
780 vapor estimated from shipborne GPS measurements, *Geophys. Res. Lett.*, **35**, L13803.

781 Hadas, T., F. N. Teferle, K. Kazmierski, P. Hardyniec, J. Bosy, 2017: Optimum stochastic
782 modeling for GNSS tropospheric delay estimation in real-time. *GPS Solutions*, **21**,
783 1069–1081. <https://doi.org/10.1007/s10291-016-0595-0>

784 Huang, C.-Y., W. H. Teng, S. P. Ho, and Y. H. Kuo, 2013: Global variation of COSMIC
785 precipitable water over land: comparisons with ground-based GPS measurements and
786 NCEP reanalyses, *Geophys. Res. Lett.*, **40**, 5327–5331.

787 Ikuta, Y., H. Seko, and Y. Shoji, 2021: Assimilation of shipborne precipitable water vapour
788 by the Global Navigation Satellite Systems for extreme precipitation events, *Quart. J.*
789 *Roy. Meteor. Soc.*, 1-19, DOI: 10.1002/qj.4192

790 Imada, Y., H. Kawase, M. Watanabe, M. Arai, H. Shiogama and I. Takayabu, 2020:
791 Advanced risk-based event attribution for heavy regional rainfall events, *npj Climatic and*
792 *Atmospheric Science*, **37**, <https://doi.org/10.1038/s41612-020-00141-y>

793 Kato, T., 2018: Representative height of the low-level water vapor field for examining the
794 initiation of moist convection leading to heavy rainfall in East Asia, *J. Meteor. Soc.*
795 *Japan*, **96**, 69-83.

796 Kato, T., Y. Terada, K. Tadokoro, N. Kinugasa, A. Futamura, M. Toyoshima, S. Yamamoto,
797 M. Ishii, T. Tsugawa, M. Nishioka, K. Takizawa, Y. Shoji, and H. Seko, 2018:
798 Development of GNSS Buoy for a Synthetic Geohazard Monitoring System, *J. Disaster*
799 *Res.*, **13**, 460-471.

800 Kato, T., 2006: Structure of the band-shaped precipitation system inducing the heavy
801 rainfall observed over northern Kyushu, Japan on 29 June 1999, *J. Meteor. Soc. Japan*,
802 **84**, 129-153.

803 Kazumori, M., 2013: Description of GCOM-W1 AMSR2 Integrated Water Vapor and Cloud
804 Liquid Water Retrieval Algorithm, Chapter 2 of “Descriptions of GCOM-W1 AMSR2 Level
805 1R and Level 2 Algorithms”, [available at
806 http://suzaku.eorc.jaxa.jp/GCOM_W/data/doc/NDX-120015A.pdf]. (accessed on March
807 26,2022)

808 Kogure, S., M. Endo, M. Miyoshi, K. Sato, K. Kawate, T. Takasu, T. Osawa, and T. Suzuki,
809 2016: Multi-GNSS Advanced Demonstration tool for Orbit and Clock Analysis
810 (MADOCA), the development result and its product utilization to automobile applications.
811 Proceedings of 2016 annual congress (spring) of the Society of Automotive Engineers of
812 Japan, 56-1. (in Japanese)

813 Kouba, J and P. Heroux, 2001: Precise point positioning using IGS orbit and clock
814 products, *GPS Solutions*, **5**,12–28

815 Lu, C., X. Li, T. Nilson, T. Ning, R. Heinkelmann, M. Ge, S. Glaser, H. Schuh, 2015: Real-
816 time retrieval of precipitable water vapor from GPS and BeiDou observations. *J Geod*,
817 **89**, 843–856.

818 Pacione, R., F. Vespe, B. Pace, 2009: Near Real-Time GPS Zenith Total Delay validation
819 at E-GVAP Super Sites, *Bollettino Di Geodesia E Scienze Affini* 1 [available at
820 [http://igs.oma.be/_documentation/papers/eurefsymposium2008/near_real_time_gps_ze
821 nith_total_delay_validation_at_e_gvap_super_sites.pdf](http://igs.oma.be/_documentation/papers/eurefsymposium2008/near_real_time_gps_zenith_total_delay_validation_at_e_gvap_super_sites.pdf)]

822 Rocken, C., J. Johnson, T. Van Hove, T. Iwabuchi, 2005: Atmospheric water vapor and
823 geoid measurements in the open ocean with GPS. *Geophys. Res. Lett.*, **32**, L12813.

824 Rothacher, M., and G. Beutler, 1998: The role of GPS in the study of global change,
825 *Physics and Chemistry of the Earth*, **23**, 1029-1040.

826 Santerre, R., 1991: Impact of GPS satellite sky distribution, *Manuscripta Geodaetica*, **16**,
827 28-53.

828 Shoji, Y., K. Sato, M. Yabuki, T. Tsuda, 2017: Comparison of shipborne GNSS-derived
829 precipitable water vapor with radiosonde in the western North Pacific and in the seas
830 adjacent to Japan, *Earth, Planets Space*, **69**, 153.

831 Shoji, Y., K. Sato, M. Yabuki, T. Tsuda, 2016: PWV Retrieval over the Ocean Using
832 Shipborne GNSS Receivers with MADOCA Real-Time Orbits. *SOLA*, **12**, 265–271.

833 Shoji, Y., 2009: A Study of Near Real-time Water Vapor Analysis using a Nationwide Dense
834 GPS Network of Japan. *J. Meteor. Soc. Japan*, **87**, 1–18.

835 Shoji, Y., M. Kunii, and K. Saito, 2009; Assimilation of Nationwide and Global GPS PWV
836 Data for a Heavy Rain Event on 28 July 2008 in Hokuriku and Kinki, Japan, *SOLA*, **5**,
837 045–048.

838 Shoji, Y., H. Nakamura, K. Aonashi, A. Ichiki, and H. Seko, 2000: Semi-diurnal and diurnal
839 variation of errors in GPS precipitable water vapor at Tsukuba, Japan caused by site
840 displacement due to ocean tidal loading. *Earth, Planets Space*, **52**, 685–690.

841 Sun P., K. Zhang, W. Suqin, W. Moufeng, L Yun, 2021: Retrieving Precipitable Water Vapor
842 from Real-Time Precise Point Positioning Using VMF1/VMF3 Forecasting Products,
843 *Remote Sensing*, **13**, 3245, <https://doi.org/10.3390/rs13163245>.

844 Takasu T., 2013: RTKLIB 2.4.2 manual, [Available at
845 http://www.rtklib.com/prog/manual_2.4.2.pdf]

846 Teng, W.-H., C.-Y. Huang, S.-P. Ho, Y.-H. Kuo, and X.-J. Zhou, 2013: Characteristics of
847 global precipitable water in ENSO events revealed by COSMIC measurements, *J.*
848 *Geophys. Res. Atmos.*, **118**, 8411–8425, doi:10.1002/jgrd.50371.

849 Tsuguti, H., and T. Kato, 2014: Contributing Factors of the Heavy Rainfall Event at Amami-
850 Oshima Island, Japan, on 20 October 2010, *J. Meteor. Soc. Japan*, **92**, 163-183.

851 Vaclavovic, P., J. Dousa, M. Elias, J. Kostelecky, 2017: Using external tropospheric
852 corrections to improve GNSS positioning of hot-air balloon, *GPS Solutions*, **21**, 1479–
853 1489. <https://doi.org/10.1007/s10291-017-0628-3>

854 Wang, G., F. Blume, C. Meertens, P. Ibanez, and M. Schulze, 2012: Performance of High-
855 Rate Kinematic GPS during Strong Shaking: Observations from Shake Table Tests and
856 the 2010 Chile Earthquake, *Journal of Geodetic Science*, **2**, 15–30, doi:10.2478/v10156-
857 011-0020-0.

858 Weiss, J.-P., W.S. Schreiner, J.J. Braun, W. Xia-Serafino, C.-Y. Huang, 2022: COSMIC-2
859 Mission Summary at Three Years in Orbit. *Atmosphere*, **13**, 1409,
860 <https://doi.org/10.3390/atmos13091409>

861 Wick, G. A., Y. H. Kuo, F. M. Ralph, T. K. Wee, and P. J. Neiman, 2008: Intercomparison of
862 integrated water vapor retrievals from SSM/I and COSMIC, *Geophys. Res. Lett.*, **35**,
863 3263–3266.

864 Xu, P., C. Shi, R. Fang, J. Liu, X. Niu, Q. Zhang, and T. Yanagidani, 2013: High-rate
865 Precise Point Positioning (PPP) to Measure Seismic Wave Motions: An Experimental
866 Comparison of GPS PPP with Inertial Measurement Units, *Journal of Geodesy*, **87**, 361–
867 372, doi:10.1007/s00190-012-0606-z.

868 Yuan, Y., K. Zhang, W. Rohm, S. Choy, R. Norman, and C.-S. Wang, 2014: Real-time
869 retrieval of precipitable water vapor from GPS precise point positioning, *J. Geophys.*
870 *Res. Atmos.*, **119**, 10,044–10,057, doi:10.1002/2014JD021486.

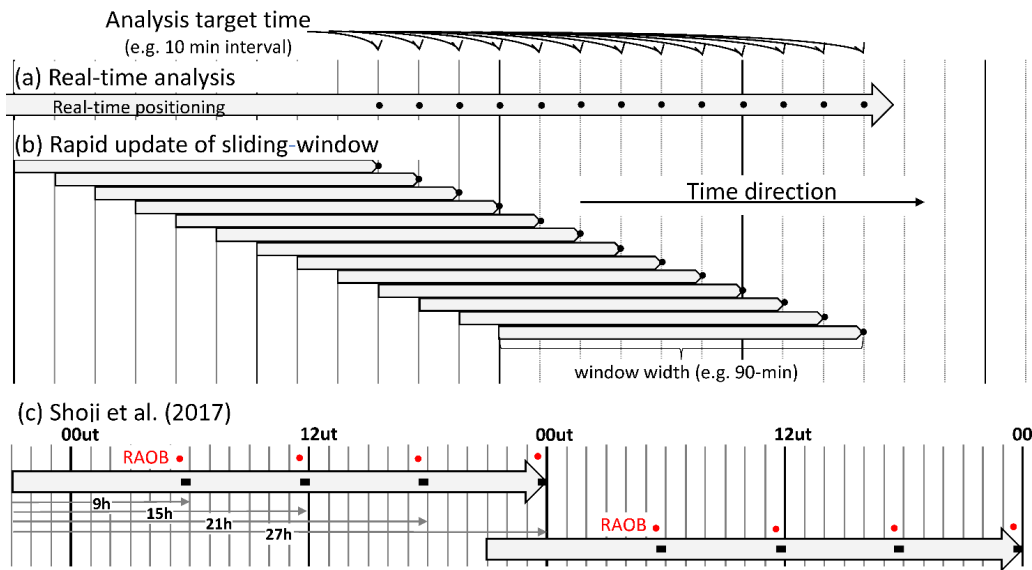
871 Zhang, Q., J. Ye, S. Zhang, and F. Han, 2018: Precipitable Water Vapor Retrieval and
872 Analysis by Multiple Data Sources: Ground-Based GNSS, Radio Occultation,
873 Radiosonde, Microwave Satellite, and NWP Reanalysis Data, *Journal of Sensors*,
874 <https://doi.org/10.1155/2018/3428303>.

875 Zhou, F-C., X. Song, P. Leng, H. Wu, B-H. Tang, 2016: An algorithm for retrieving
876 precipitable water vapor over land based on passive microwave satellite data. *Adv.*
877 *Meteor.*, **2016**, 1–11, <https://doi.org/10.1155/2016/4126393>.

878 Zumberge, J. F., M. B. Heflin, D. C. Jefferson, and M. M. Watkins, 1997: Precise point
879 positioning for the efficient and robust analysis of GPS data from large networks. *J.*
880 *Geophys. Res.*, **102**, 5005–5017.

881

List of Figures



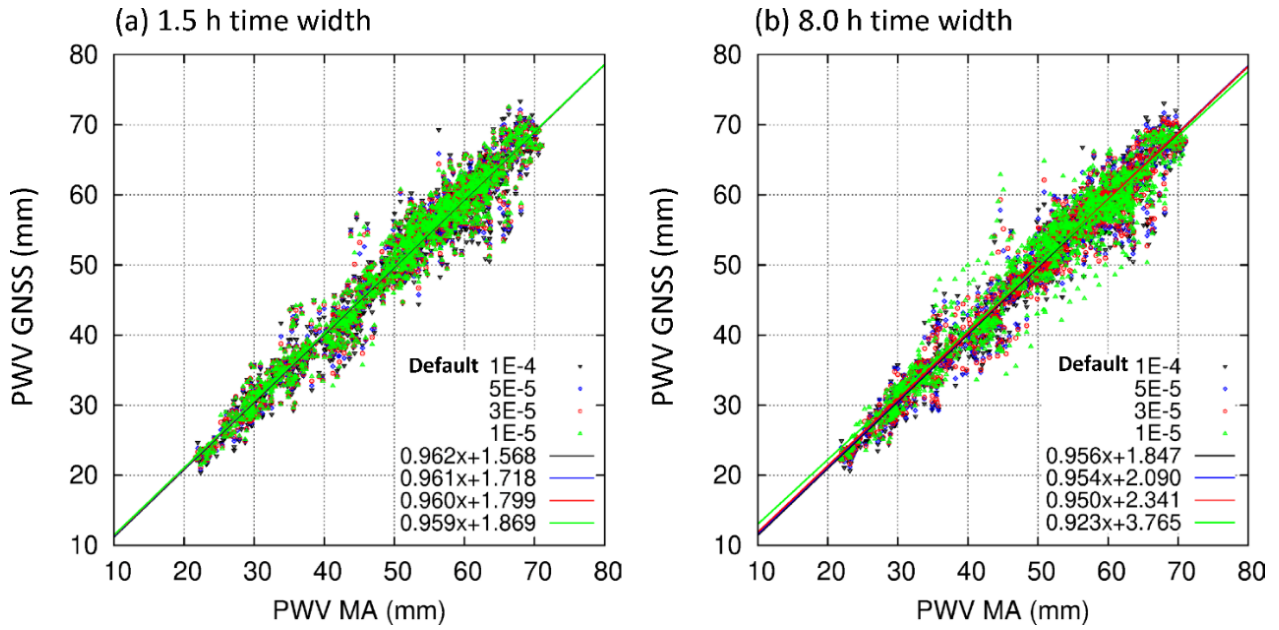
884 Fig. 1. Schematic illustration of two procedures of real-time analysis: (a) true real-time
 885 analysis and (b) rapid update of sliding window, and (c) post processing adopted by
 886 Shoji et al. (2017).

887 In (b), the final (latest) time of the positioning analysis is the target time of the analysis.

888 However, in (a) and (c), the target times of PWV analyses are within each GNSS
 889 analysis. In (c), data within 3 h from the start of each 27-h batch analysis were discarded
 890 to use well-converged results only; all the remaining 24-h results were treated as
 891 evaluation targets.

892 In Shoji et al. (2017) and this study, when comparing with RAOB PWV, GNSS-derived
 893 PWV averaged 30 min from each RAOB launch time. For example, when compared with
 894 a RAOB launched at 11:30 UTC or 23:30 UTC, the GNSS-derived PWV is the 30 min
 895 average value from 14.5 to 15 h or 26.5 to 27 h after the analysis start time, respectively.

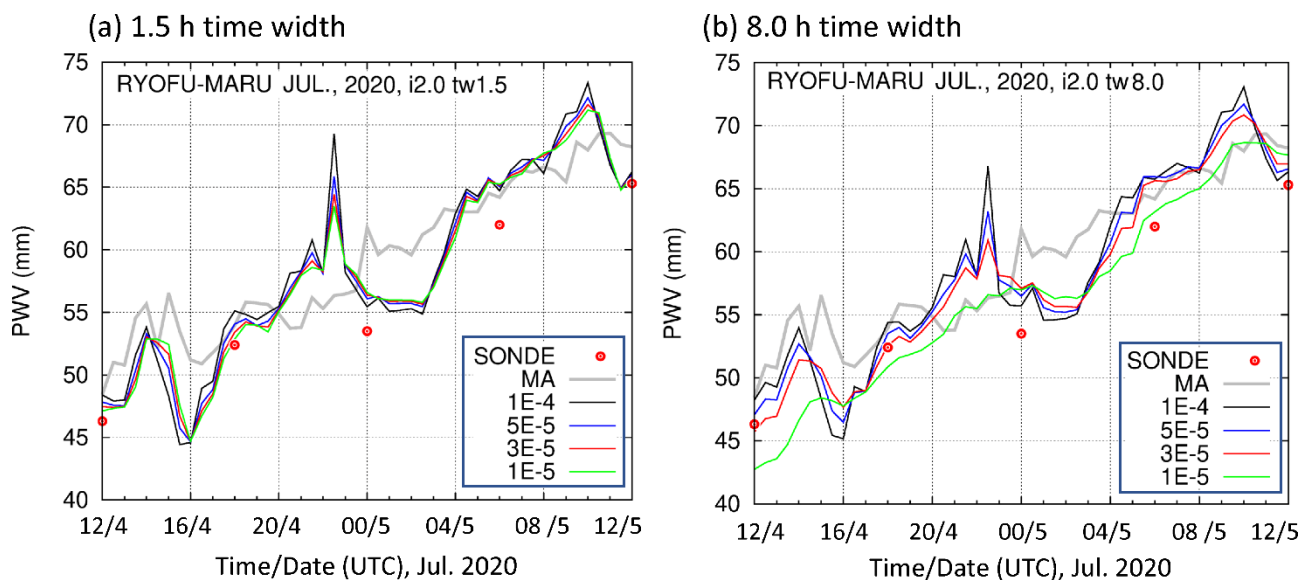
896



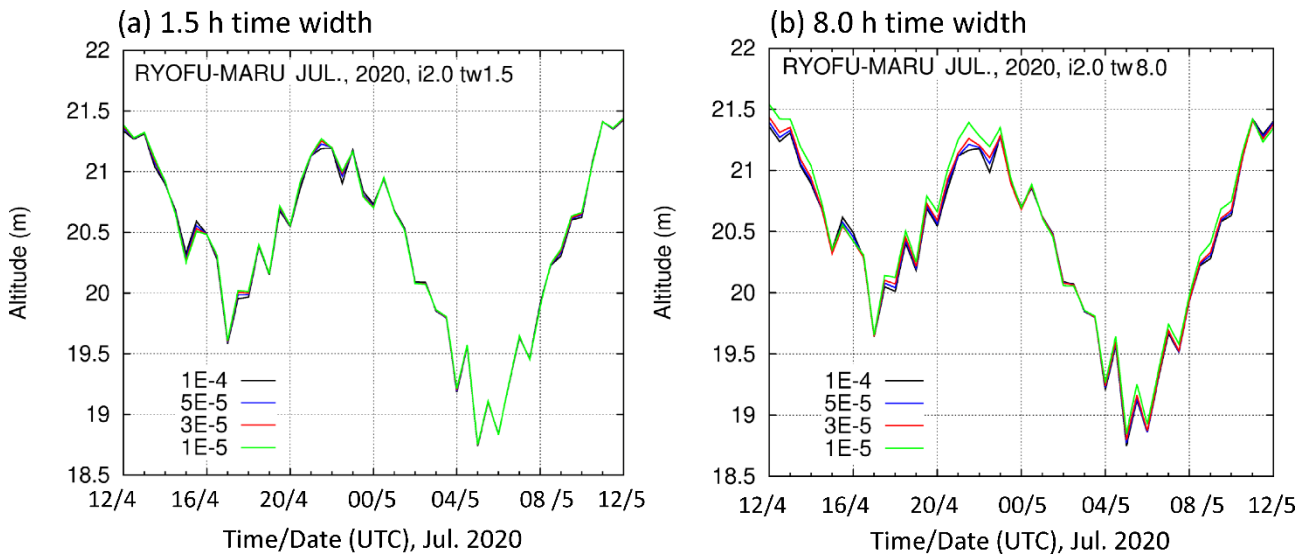
897 Fig. 2. Scatter diagram of PWV comparing MA and ship-based GNSS, in a (a) 1.5 h and
898 (b) 8.0 h widths. GNSS-derived PWVs are plotted with different colors depending on
899 RWPN sigma, as 1.0×10^{-4} (black), 5.0×10^{-5} (blue), 3.0×10^{-5} (red), and 1.0×10^{-5}
900 (green) $\text{m s}^{-1/2}$.

901

902



903 Fig. 3. The 24 h PWV sequence at Ryofu Maru from 12:00 UTC July 4 to 12:00 UTC July
 904 5, 2020. The (a) 1.5 h and (b) 8.0 h widths are shown. Gray lines represent MA, while red
 905 dots represent RAOB. GNSS-derived PWVs are plotted with different colors depending on
 906 RWPN sigma as 1.0×10^{-4} (black), 5.0×10^{-5} (blue), 3.0×10^{-5} (red), and 1.0×10^{-5} (green)
 907 $\text{m s}^{-1/2}$.
 908



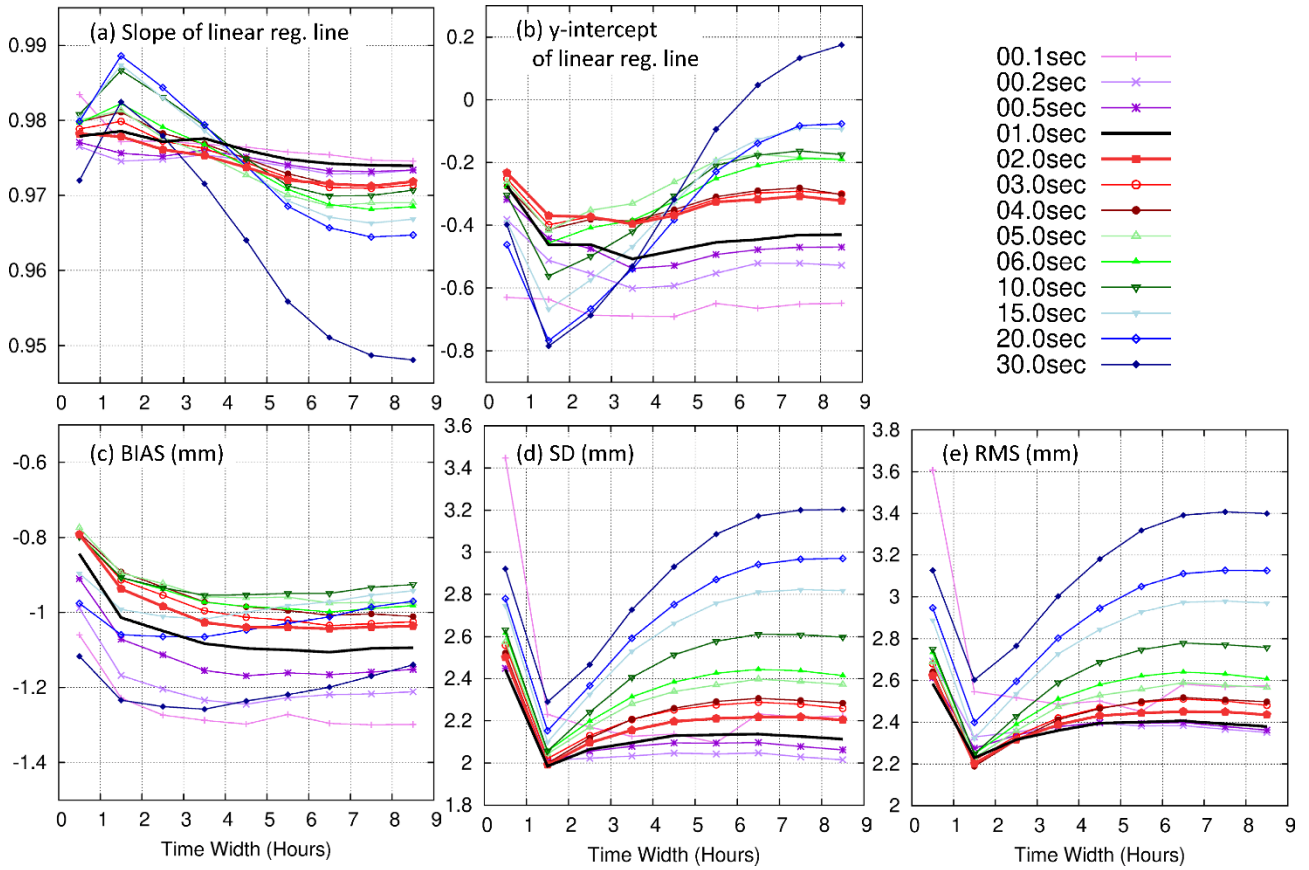
910

911 Fig. 4. The 24 h sequence of altitude at RYOFU MARU GNSS antenna from 12:00 UTC

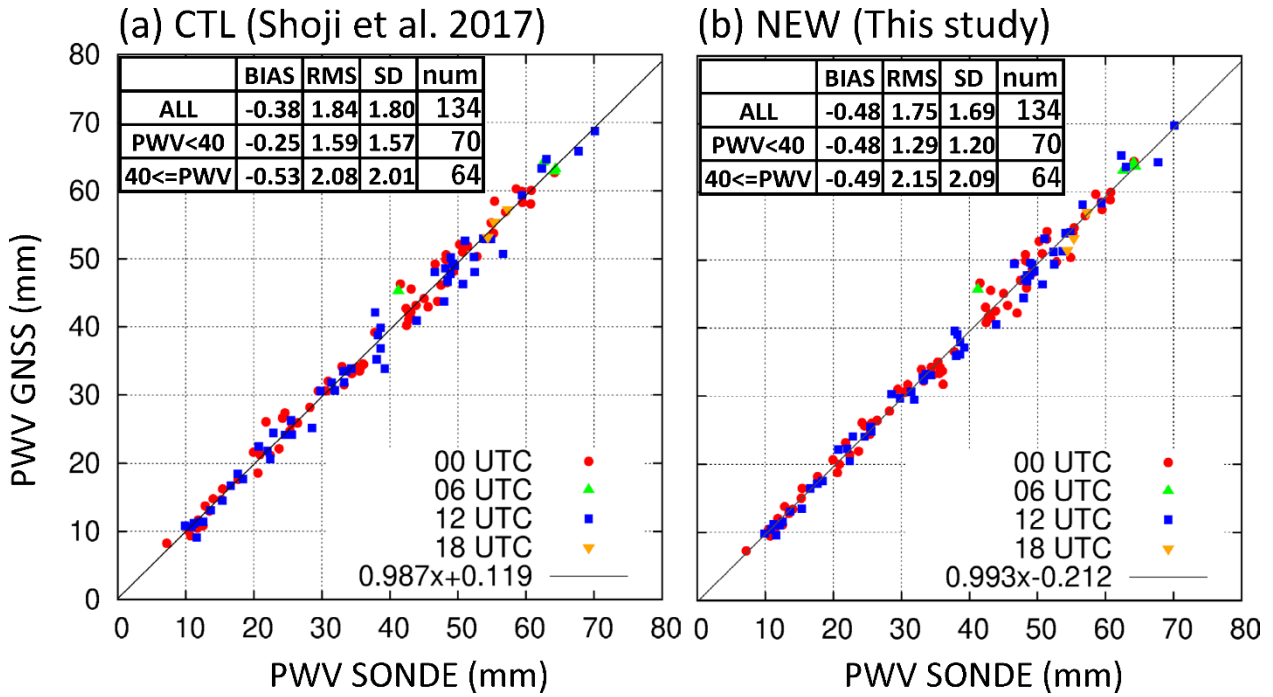
912 July 4 to 12:00 UTC July 5, 2020. The (a) 1.5 h and (b) 8.0 h widths are shown. Lines

913 are plotted with different colors depending on RWPN sigma as 1.0×10^{-4} (black), $5.0 \times$

914 10^{-5} (blue), 3.0×10^{-5} (red), and 1.0×10^{-5} (green) $\text{m s}^{-1/2}$.



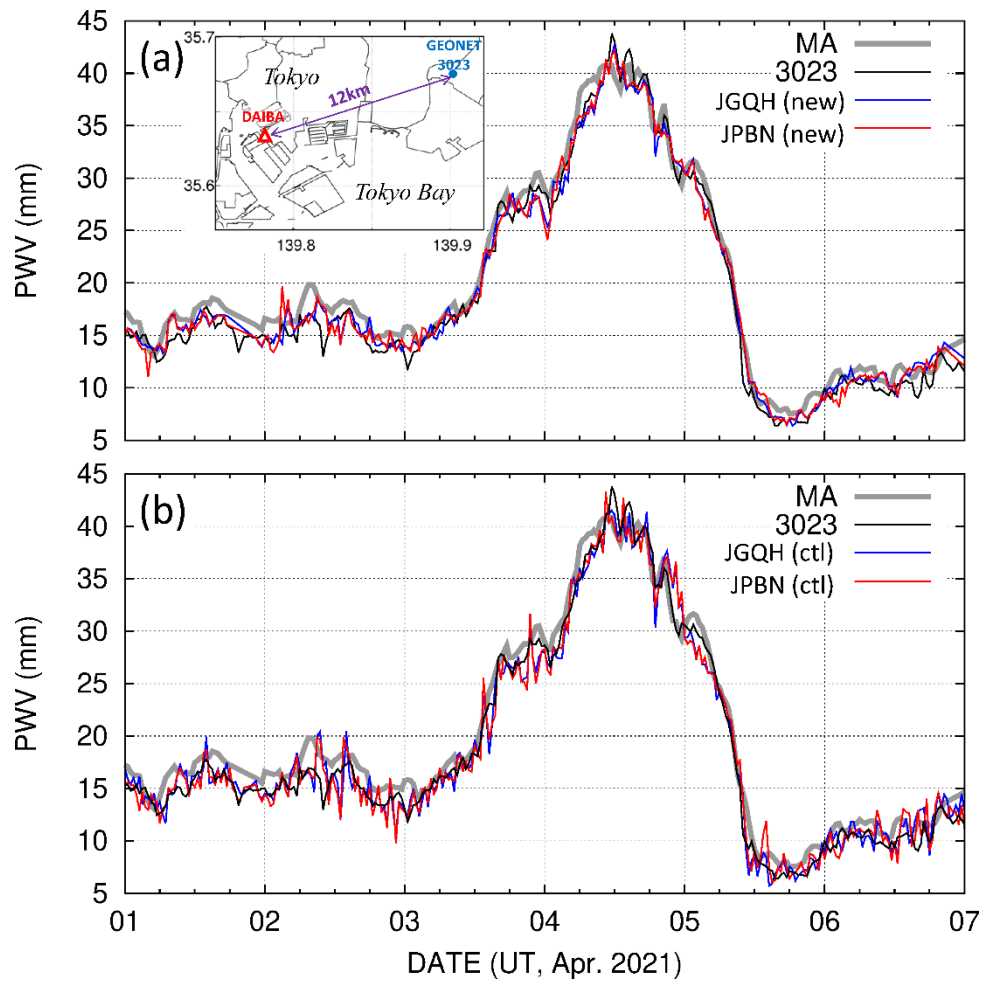
916 Fig. 5. Differences in ship-based GNSS-derived PWV comparison against MA caused by
917 different time widths of sliding windows (x-axis) and different update intervals (line color).
918 (a) The regression coefficient of the linear regression line, (b) y-intercept of the linear
919 regression line, (c) bias, (d) SD, and (e) RMS. Lines are plotted with different colors
920 depending on the update interval.



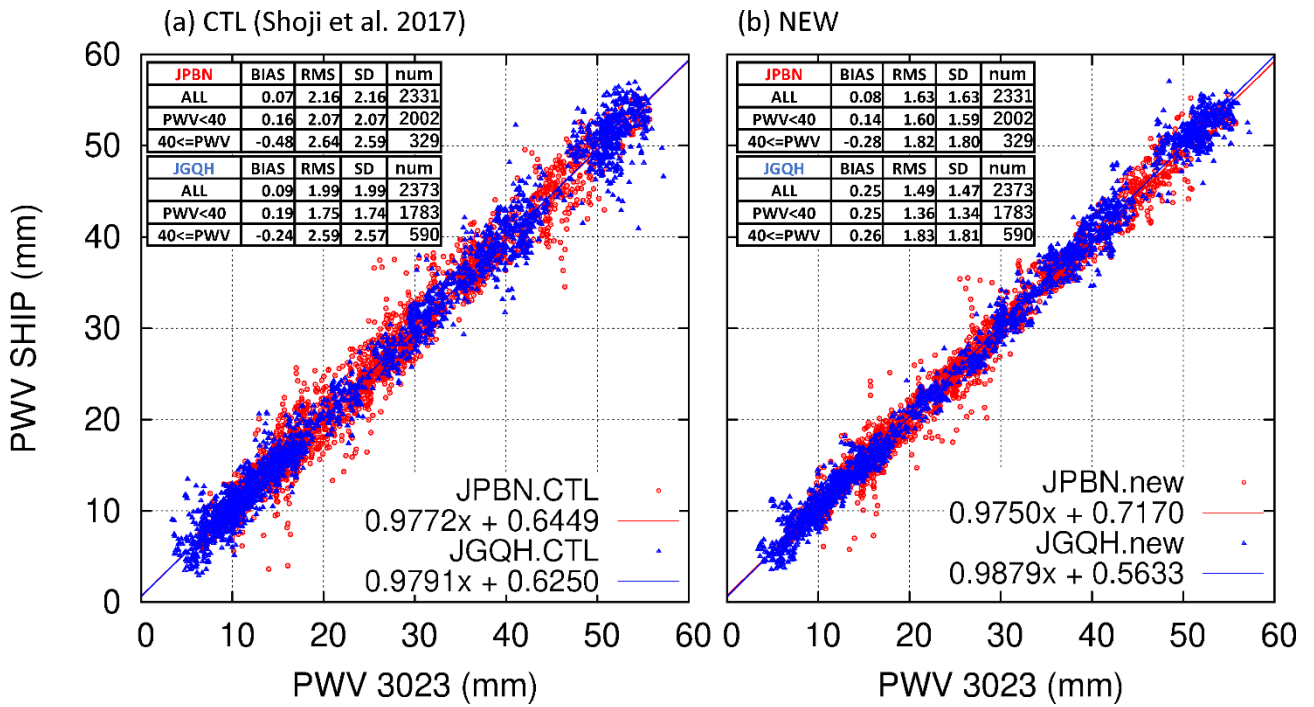
923 Fig. 6. PWV comparison results obtained from Ryofu Maru observations in 2019 and 2020.

924 In (a), the GNSS-derived PWV is retrieved using the procedure of Shoji et al. (2017),
 925 while the GNSS-derived PWV is retrieved by using our new settings, as shown in (b).

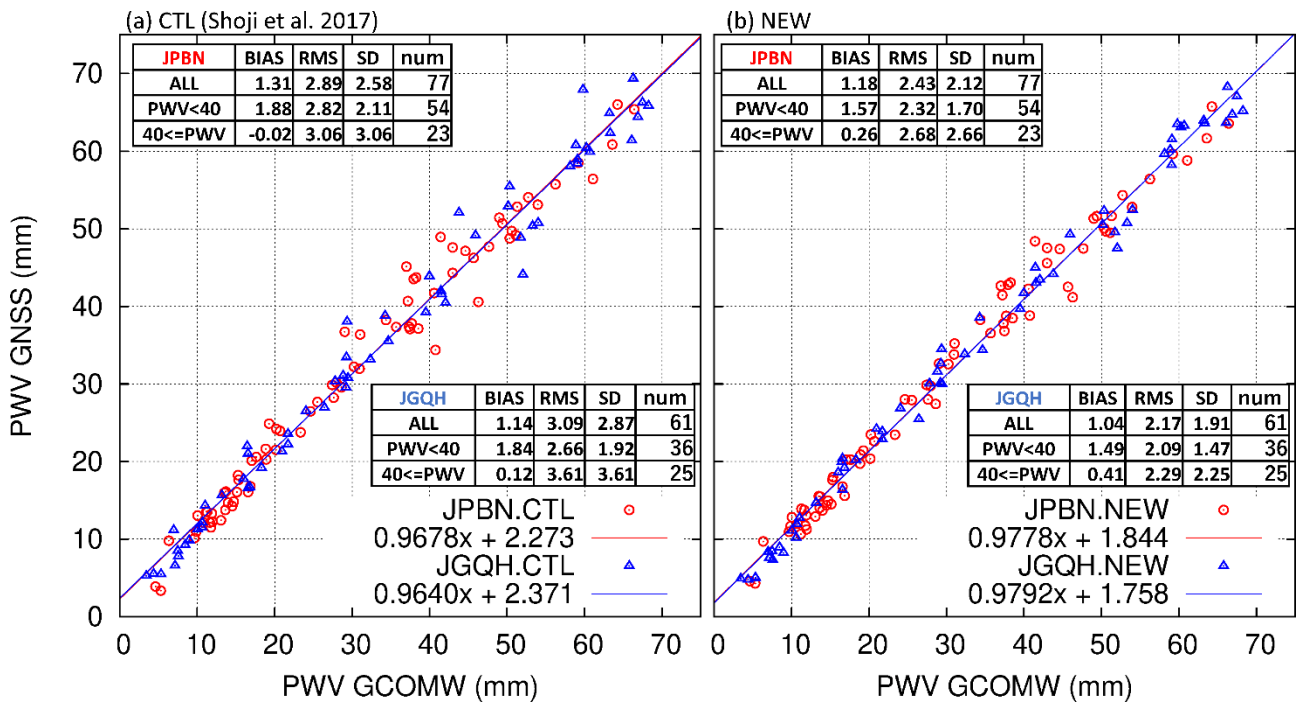
926 Black lines are linear regression lines.



929 Fig. 7. The PWV time sequence for April 1–April 6, 2021. Gray thick line: MA. Black line:
 930 3023 (nearby fixed GNSS station). Blue line: Ryofu Maru (JGQH); Red line: Keifu Maru
 931 (JPBN). All-time series are drawn using data at 30-min intervals. The time sequences of
 932 JGQH and JPBN in (a) are obtained by the new settings described in this study, while
 933 those in (b), written as CTL, are obtained by those of Shoji et al. (2017). During this
 934 period, the two vessels were anchored side by side at their home port (Daiba, Minato
 935 Ward, Tokyo). The GEONET station 3023 (Chiba Ichikawa) is located approximately 12
 936 km ENE from JGQH and JPBN.



938 Fig. 8. PWV comparison between a ground-fixed GNSS station (3023) and ship-based
 939 GNSS on JPBN (red circles) and JGQH (blue triangles). Comparisons were made
 940 between April 1 to July 22, 2021, when each vessel was located within 15 km of the
 941 “3023” station. Linear regression lines are also plotted with red and blue lines.

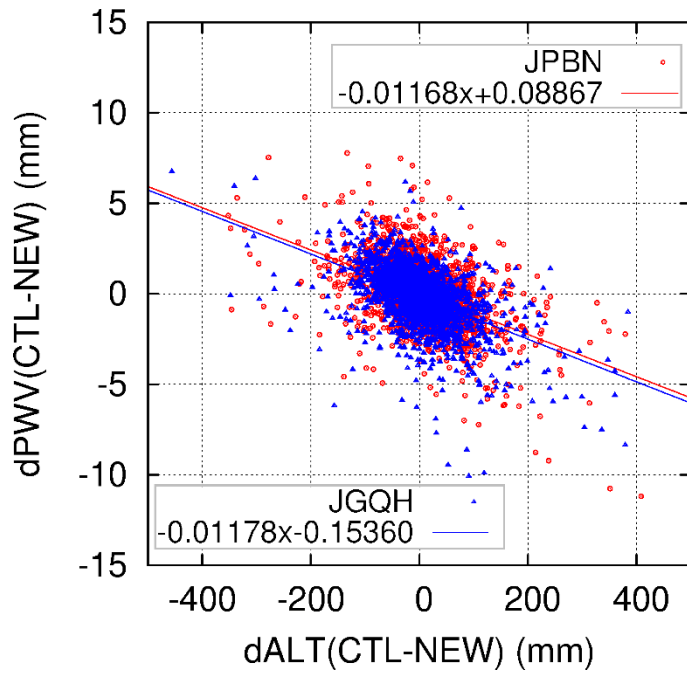


943

944 Fig. 9 GCOM-W1/AMSR2 with ship-based GNSS-derived PWV on JPBN (red circles) and
 945 JGQH (blue triangles). Comparisons were made between April 1 to July 22, 2021. When
 946 making comparisons, time differences of up to 5 minutes and differences in location
 947 within a distance of 20 km were allowed. Linear regression lines are also plotted with red
 948 and blue lines.

949

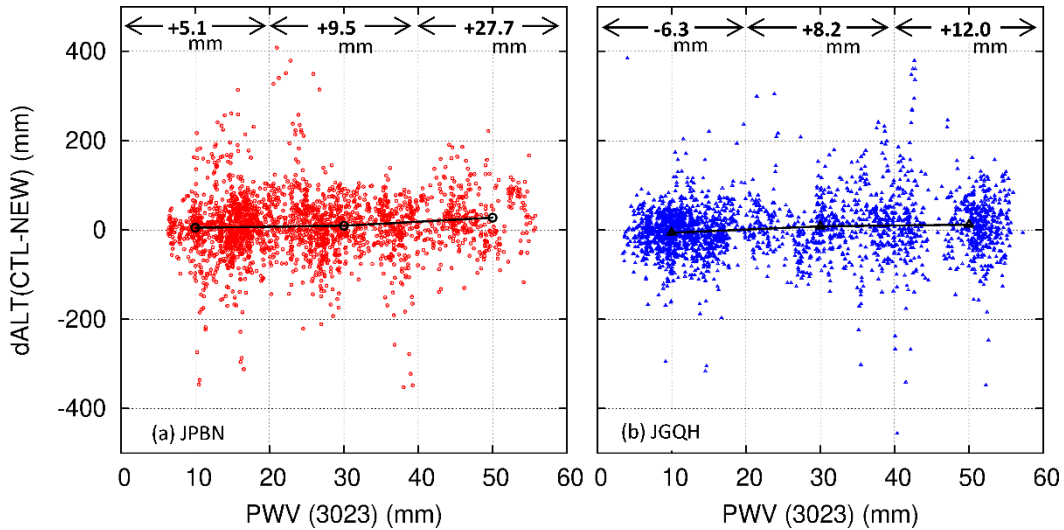
950



951 Fig. 10. Scatter plot and linear regression lines of the difference in analyzed altitude (CTL-
952 NEW) versus the difference in PWV for the data plotted in Fig. 8

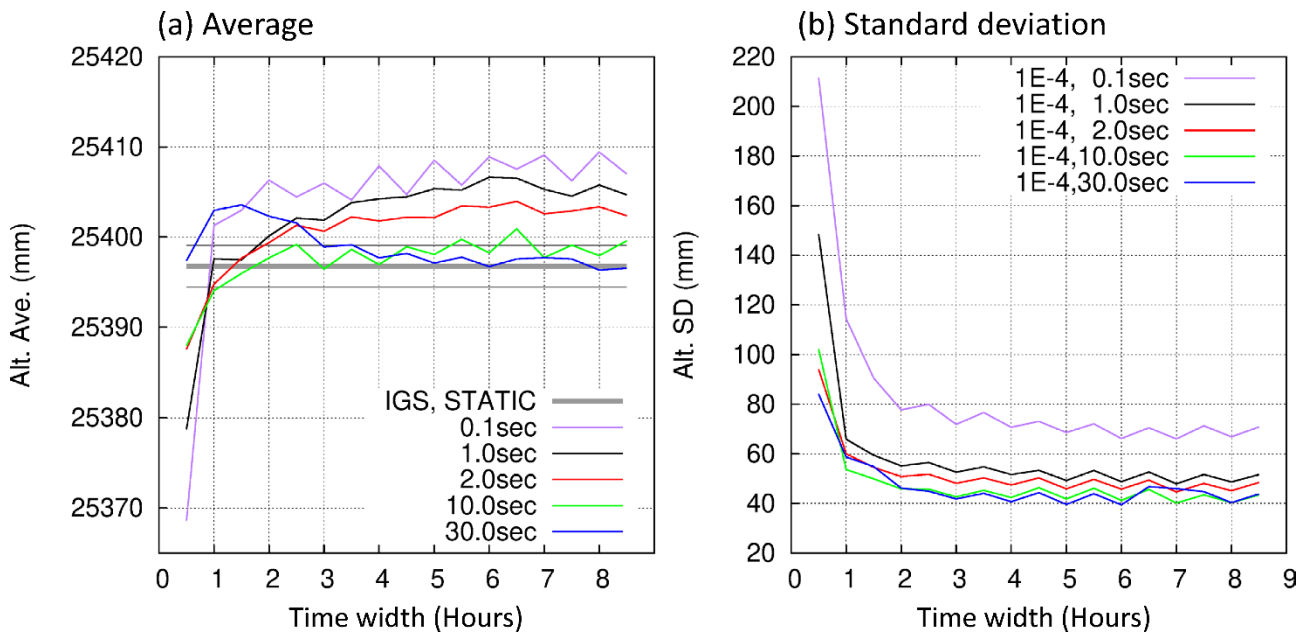
953

954

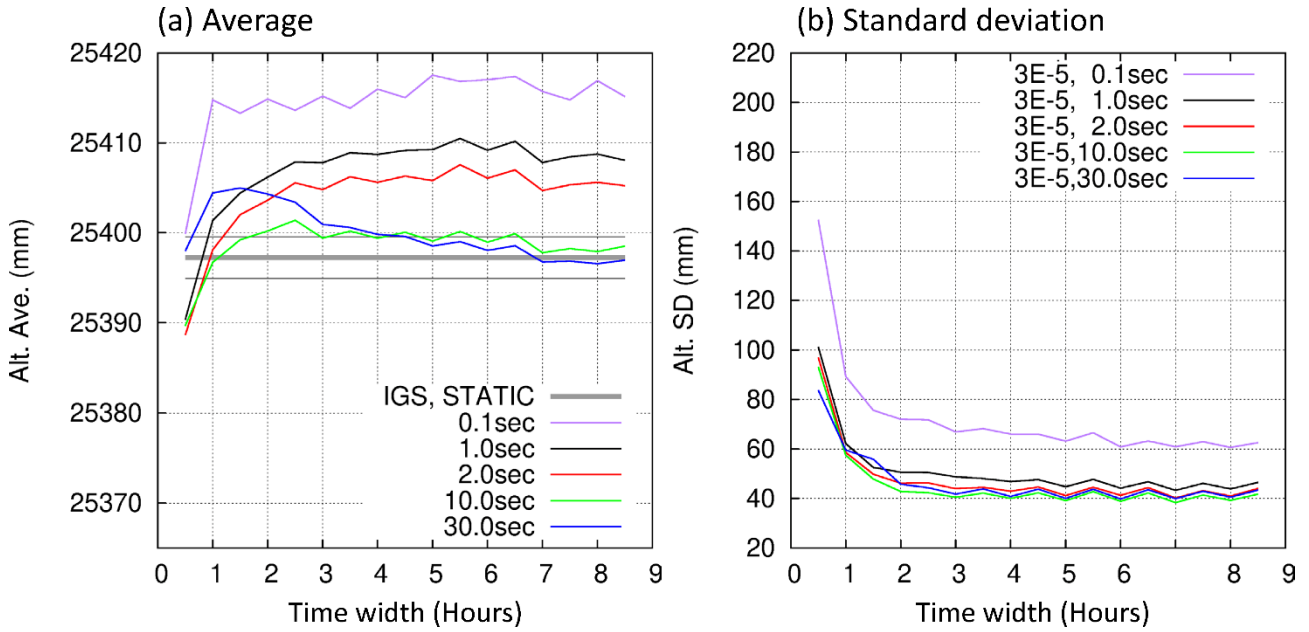


955 Fig. 11. Differences in the analyzed GNSS antenna altitude using the settings of CTL and
956 NEW (CTL-NEW) for the data plotted in Fig. 8. (a) JPBN and (b) JGQH.

957



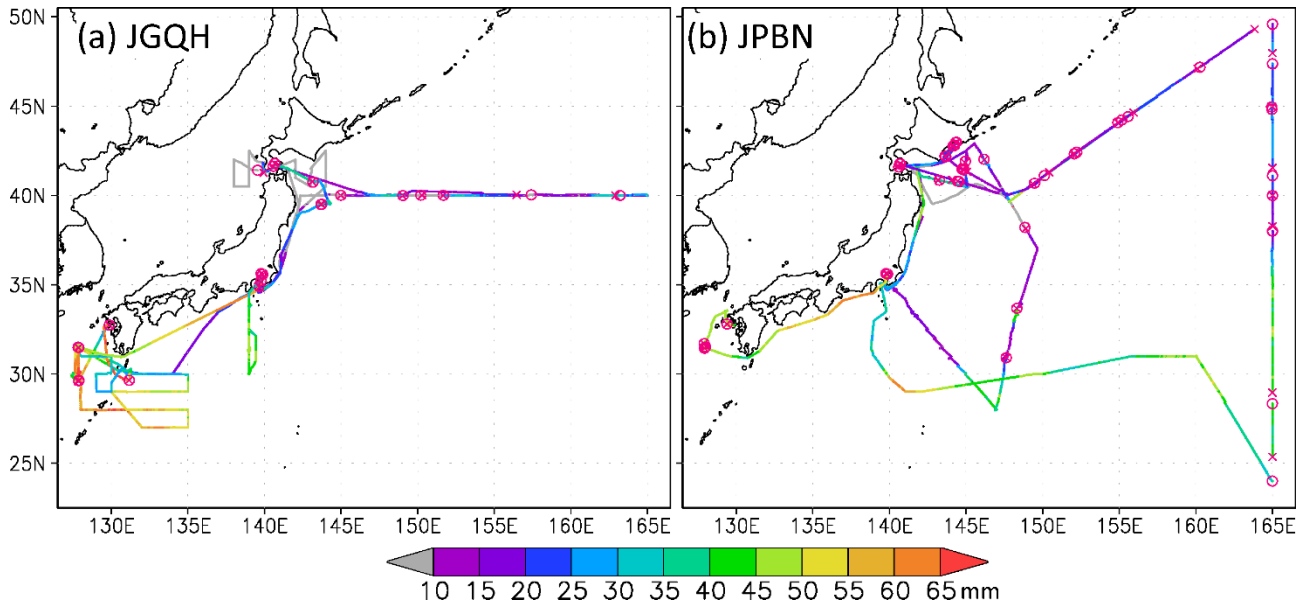
958 Fig. 12. Average and SD of analyzed altitudes of a fixed GNSS station at the
 959 Meteorological Research Institute (Tsukuba, Ibaraki, Japan) by kinematic PPP applying
 960 the default value of RWPN, $1.0 \times 10^{-4} \text{ m s}^{-1/2}$, for 16 d from December 1 to 16, 2020. In
 961 Panel (a), a thick gray horizontal line is the average of the daily analyzed altitudes
 962 (25396.77 mm) estimated by the static PPP applying the IGS precise ephemeris (IGF).
 963 The two black horizontal lines above and below the thick gray horizontal line indicate the
 964 altitude of the average ± 2.31 mm SD.
 965



967 Fig. 13. Same as Fig. 12 except the RWPN is $3.0 \times 10^{-5} \text{ m s}^{-1/2}$. In Panel (a), a thick gray
 968 horizontal line is the average of the daily analyzed altitudes (25397.25 mm) estimated by
 969 the static PPP applying the IGF. The two black horizontal lines above and below the
 970 thick gray horizontal line indicate the altitude of the average $\pm 2.32 \text{ mm SD}$.

972

973

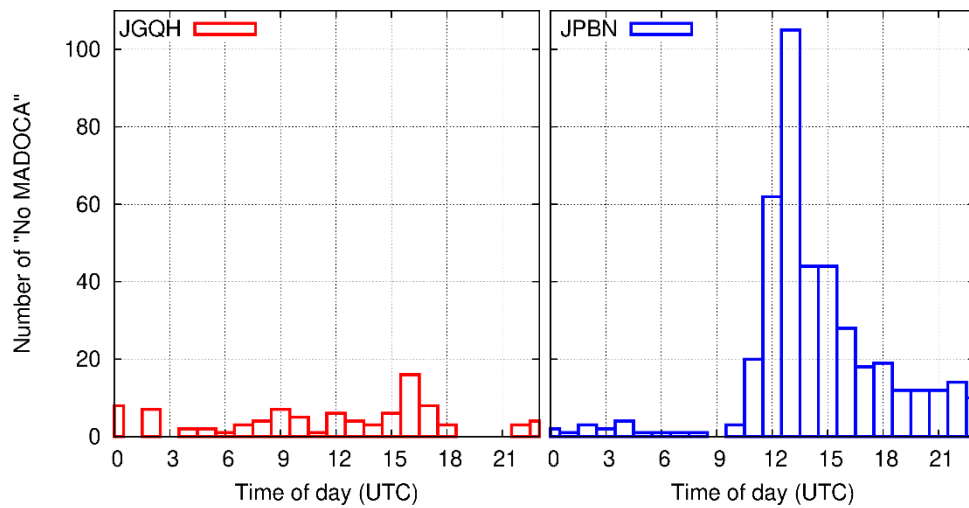


974 Fig. A1. Estimated GNSS-derived PWV along the trajectories of (a) Ryofu Maru (JGQH)

975 and (b) Keifu Maru (JPBN). Pairs of red crosses and red circles are the start and

976 endpoints of MADOCA acquisition failure.

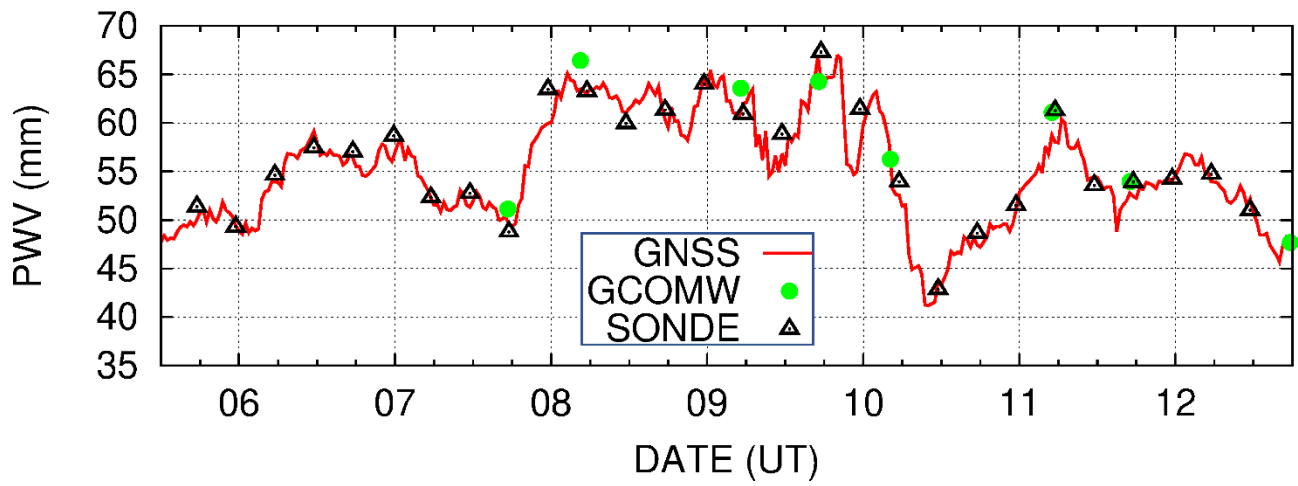
977



978 Fig. A2. Histogram of the number of MADOCA acquisition failures for the bins of time of

979 day.

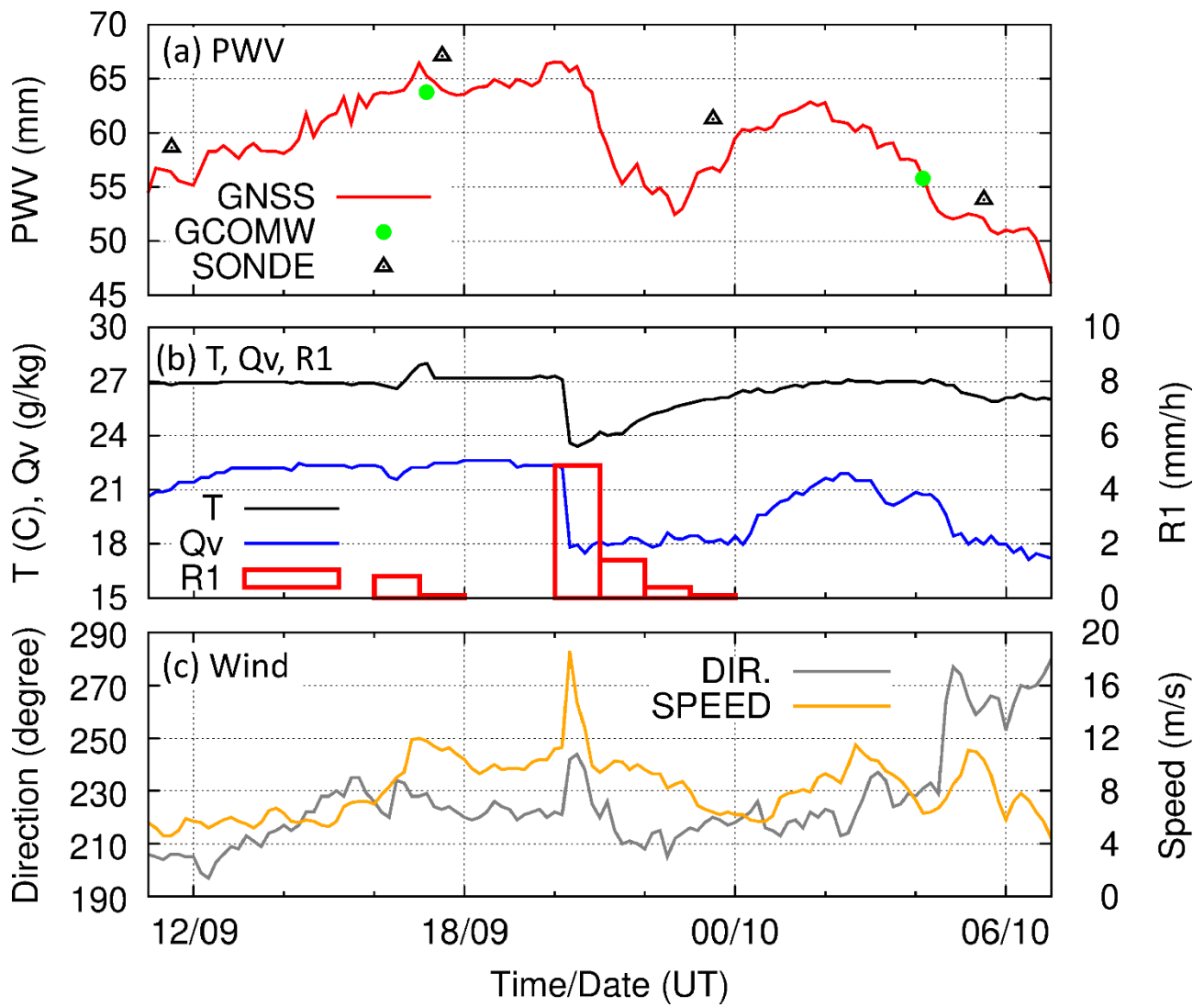
980



981 Fig. A3 PWV sequence at Keifu Maru (JPBN) from July 5 to 12, 2021 (red line: GNSS;

982 green circles: GCOM-W1; black open triangles: RAOB).

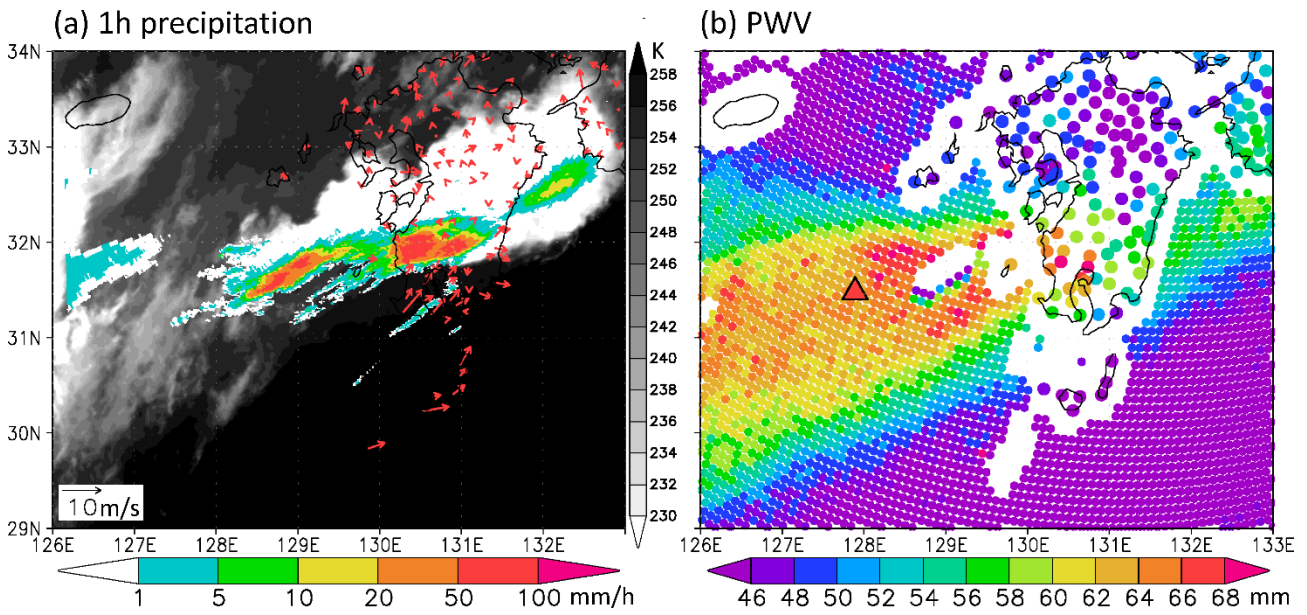
983



984 Fig. A4. The 20 h time sequences of (a) PWV, (b) temperature, water vapor mixing ratio, 1
 985 h precipitation, and (c) wind observed on Keifu Maru from 11:00 July 9 to 07:00 July 10,
 986 2021.

987

988



989

990 Fig. A5. Distribution of (a) radar/rain gauge analyzed precipitation (color shade), 7.3 μm
991 band TBB by GMS HIMAWARI8 (gray shade), and surface wind (red vector), and (b)
992 PWV analyzed from ground-based GNSS stations (larger dots on land), from GCOM-W1
993 (smaller dots over the ocean) and Keifu Maru (triangle) at 17:00UTC on July 9, 2021.

994

995

996

997

List of Tables

998

999

Table 1. Main specifications of the GNSS analyses.

Classification	Specification	Remarks
Software	RNX2RTKP (RTKLIB ver. 2.4.3, b33)	
Analysis procedure	Kinematic Precise Point Positioning	
Integer ambiguity	Continuously estimated	
Ephemeris	MADOCA real-time product	
Mapping function	GMF	Boehm et al. 2006
Elevation cut-off angle	3°	
Antenna phase center variation	igs14.atx	https://files.igs.org/pub/station/general/igs14.atx Shoji et al. 2017: igs08.atx
Ionosphere correction	Ionosphere-free linear combination	
Time-dependent parameters	<ul style="list-style-type: none"> • Antenna coordinate • Receiver clock • Zenith Total Delay • Tropospheric gradient 	
Random-walk process noise sigma of ZTD	The following values were used for evaluation: 1 x 10 ⁻⁴ , 5 x 10 ⁻⁵ , 3 x 10 ⁻⁵ , 1 x 10 ⁻⁵ m/s ^{^(1/2)}	Default : 1 x 10 ⁻⁴ m/s ^{^(1/2)} Shoji et al. 2017: 1 x 10 ⁻⁴ m/s ^{^(1/2)}
Width of the sliding-window or batch-analysis	The following time lengths were used for evaluation: 0.5, 1.5, 2.5, 3.5, 4.5, 5.5, 6.5, 7.5, and 8.5 h	Shoji et al. 2017: 27 h (see Fig. 1(c) for detail)
Update interval of the time-dependent parameters	The following intervals were used for evaluation: 0.1, 0.2, 0.3, 0.4, 0.5, 1, 2, 3, 4, 5, 6, 10, 15, 20, and 30 s	Shoji et al. 2017: 1 s

1000

1001

Table 2. RWPN used in previous studies.

Article	Original Text	In the same unit of m/\sqrt{s}
Bar-Sever et al. 1998	10.2 mm/ \sqrt{h}	17.0 × 10 ⁻⁵
Kouba and Heroux 2001	5 mm/ \sqrt{h}	8.3 × 10 ⁻⁵
Pacione et al. 2009	20 mm/ \sqrt{h}	33.3 × 10 ⁻⁵
Yuan et al. 2014	3E ⁻⁶ m/ \sqrt{s}	0.3 × 10 ⁻⁵
Lu et al. 2015	5~10 mm/ \sqrt{h}	8.3~16.7 × 10 ⁻⁵
Sun et al 2021	0.02 mm/ \sqrt{s}	2.0 × 10 ⁻⁵
RTKLIB default	1E ⁻⁴ m/ \sqrt{s}	10.0 × 10 ⁻⁵

1002

1003

1004 Table 3. Vessels, GNSS antenna, and receiver used for the analysis optimization
 1005 experiment and observation period.

SHIP	Ryofu Maru	Wakanatsu	Ryuunan
Affiliation	Japan Meteorological Agency	RYUKYU KAIUN KAISHA	MKKLINE CO.,LTD
Type	Research vessel	Cargo ship (roll-on/roll-off)	Cargo ship
Gross Tonnage (t)	1,380	10,185	749
Length (m)	82.0	168.71	98.4
GNSS Antenna	Trimble Zephyr III		
GNSS Receiver	Trimble Alloy		
Evaluation Period (Year 2020)	Jun. 15. – Jul. 15	Oct. 22 – Nov. 20	
Sampling Interval of GNSS Observation	1 Hz	10 Hz	
GNSS antennas			

1006

1007

1008 Table 4. BIAS, RMS, and standard deviation (SD) of ship-based GNSS derived PWV
 1009 against those by MA. The (a) 1.5 h and (b) 8.0 h time width. The values are plotted with
 1010 different color depending on RWPN sigma as 1×10^{-4} (black), 5×10^{-5} (blue), 3×10^{-5}
 1011 (red), and 1×10^{-5} (green) $\text{m s}^{-1/2}$.

(a) 1.5 h time width

PWV MA	RWPN $\text{m/s}^{(1/2)}$	BIAS mm	RMS mm	SD mm	num
ALL	1×10^{-4}	-0.32	2.78	2.77	1321
	5×10^{-5}	-0.24	2.67	2.66	
	3×10^{-5}	-0.21	2.66	2.65	
	1×10^{-5}	-0.19	2.69	2.69	
< 40	1×10^{-4}	0.40	2.26	2.21	282
	5×10^{-5}	0.48	2.15	2.10	
	3×10^{-5}	0.52	2.14	2.08	
	1×10^{-5}	0.56	2.16	2.09	
≥ 40	1×10^{-4}	-0.52	2.91	2.86	1039
	5×10^{-5}	-0.44	2.79	2.76	
	3×10^{-5}	-0.41	2.79	2.76	
	1×10^{-5}	-0.39	2.82	2.79	

(b) 8.0 h time width

PWV MA	RWPN $\text{m/s}^{(1/2)}$	BIAS mm	RMS mm	SD mm	num
ALL	1×10^{-4}	-0.38	2.78	2.76	1321
	5×10^{-5}	-0.23	2.68	2.67	
	3×10^{-5}	-0.19	2.69	2.68	
	1×10^{-5}	-0.15	3.33	3.32	
< 40	1×10^{-4}	0.45	2.38	2.34	282
	5×10^{-5}	0.54	2.20	2.13	
	3×10^{-5}	0.60	2.09	2.00	
	1×10^{-5}	1.04	2.57	2.34	
≥ 40	1×10^{-4}	-0.61	2.88	2.82	1039
	5×10^{-5}	-0.43	2.79	2.76	
	3×10^{-5}	-0.47	2.84	2.81	
	1×10^{-5}	-0.46	3.50	3.47	

1012

1013 Table 5. Differences in mean PWV calculated by applying the mean altitude differences to
 1014 the regression equations in Fig. 10.

Ship	Averaged PWV range (mm)	a	b	Mean dALT (mm)	dPWV ($a \cdot \text{dALT} + b$) (mm)
JPBN	00-40	-0.01168	0.08867	7.32	0.003
	40-60			27.74	-0.235
JGQH	00-40	-0.01178	-0.15360	-1.18	-0.140
	40-60			12.01	-0.295

1015

1016

1017 Table A1. Vessels, GNSS antenna and receiver, and laptop PC, used for the real-time
 1018 operation.

SHIP	RYOFU MARU	KEIFU MARU
CALL SIGN	JGQH	JPBN
Affiliation	Japan Meteorological Agency	
Type	Research vessel	
Gross Tonnage (t)	1,380	1,483
Length (m)	82.0	82.0
GNSS Antenna	Trimble Zephyr III	Septentrio PolaNt-x MF
GNSS Receiver	CORE Chronosphere-L6	
Laptop PC	Panasonic Let's note (CPU: Intel Core i5-1135G7, Memory 16GB)	
Observation Period	26 Mar. 2021 –	
GNSS antennas		
GNSS receiver and PC		

1019

1020

1021 Table A2. Number and percentage of succeeded and unsuccessful real-time PWV analysis
 1022 from April 1 to July 22, 2021. The source of “Unexpected outage of MADOCA real-time
 1023 analysis” is https://www.gpas.co.jp/en/unyo_gpas.php.

Category	STATE	JGQH	JPBN
Analyzed	PWV calculated	16001 (98.34 %)	15824 (97.25 %)
Missed	Unexpected outage of MADOCA real-time analysis	17 (0.10 %)	
	Acquisition failure of L6E (MADOCA)	76 (0.47 %)	402 (2.47 %)
	Unexpected PC sleep	119 (0.73 %)	0 (0.00 %)
	System maintenance	59 (0.36 %)	29 (0.18 %)

1024